Cretaceous seamounts along the continent–ocean transition of the Iberian margin: U–Pb ages and Pb–Sr–Hf isotopes

Renaud Merle [a,b,*], Urs Schärer [a], Jacques Girardeau [b], Guy Cornen [b]

[a] *Laboratoire de Géochronologie, Géosciences Azur UMR-CNRS 6526, parc Valrose, F-06108 Nice, France*
[b] *Laboratoire de Planétologie et Géodynamique, UMR-CNRS 6112, Université de Nantes, 2 rue de la Houssinière, F-44322 Nantes cedex 3, France*

Abstract

To elucidate the age and origin of seamounts in the eastern North Atlantic, 54 titanite and 10 zircon fractions were dated by the U–Pb chronometer, and initial Pb, Sr, and Hf isotope ratios were measured in feldspars and zircon, respectively. Rocks analyzed are essentially trachy-andesites and trachytes dredged during the "Tore Madeira" cruise of the *Atalante* in 2001. The ages reveal different pulses of alkaline magmatism occurring at 104.4 ± 1.4 (2σ) Ma and 102.8 ± 0.7 Ma on the Sponge Bob seamount, at 96.3 ± 1.0 Ma on Ashton seamount, at 92.3 ± 3.8 Ma on the Gago Coutinho seamount, at 89.3 ± 2.3 Ma and 86.5 ± 3.4 Ma on the Jo Sister volcanic complex, and at 88.3 ± 3.3 Ma, 88.2 ± 3.9, and 80.5 ± 0.9 Ma on the Tore locality. No space–time correlation is observed for alkaline volcanism in the northern section of the Tore-Madeira Rise, which occurred 20–30 m.y. after opening of the eastern North Atlantic. Initial isotope signatures are: 19.139–19.620 for $^{206}Pb/^{204}Pb$, 15.544–15.828 for $^{207}Pb/^{204}Pb$, 38.750–39.936 for $^{208}Pb/^{204}Pb$, 0.70231–0.70340 for $^{87}Sr/^{86}Sr$, and +6.9 to +12.9 for initial epsilon Hf. These signatures are different from Atlantic MORB, the Madeira Archipelago and the Azores, but they lie in the field of worldwide OIB. The Cretaceous seamounts therefore seem to be generated by melts from a OIB-type source that interact with continental lithospheric mantle lying formerly beneath Iberia and presently within the ocean–continent transition zone. Inheritance in zircon and high ^{207}Pb of initial Pb substantiate the presence of very minor amounts of continental material in the lithospheric mantle. A long-lived thermal anomaly is the most plausible explanation for alkaline magmatism since 104 Ma and it could well be that the same anomaly is still the driving force for tertiary and quaternary alkaline magmatism in the eastern North Atlantic region. This hypothesis is agreement with the plate-tectonic position of the region since Cretaceous time, including an about 30° anti-clockwise rotation of Iberia.

1. Introduction

The seamounts studied lie in the northern and central part of the Tore-Madeira Rise, which extends over about 1000 km in SW–NE direction, roughly matching the oldest, approximately 125–130 Ma old Atlantic magnetic anomaly of oceanic crust in this region (Fig. 1; J anomaly; Pitman and Talwani, 1972; Gradstein et al., 2004). Several hypothesis were put forward to explain the origin of the rise; however, none of them is sufficiently supported by geochronological and geochemical data. Earlier explanations are: (1) emplacement of late tertiary to recent magmas em-placed along shear zones, related to N–S compression of the Iberian margin (Van der Linden, 1979; Geldmacher et al., in press), (2) volcanism occurring in relation to first oceanic lithosphere creation at 130–125 Ma, as suggested by its vicinity with the oldest Atlantic oceanic magnetic anomaly (Tucholke and Ludwig, 1982; Peirce and Barton, 1991; Olivet, 1996; Girardeau et al., 1998; Geldmacher et al., in press), (3) volcanism, ascribed to the accumulation of magmas underneath an unusually slow Atlantic ridge (Olivet, 1996; Girardeau et al., 1998), and (4) magmatism related to a "hot-spot-like" feature, active coevally with spreading (Tucholke and Ludwig, 1982; Peirce and Barton, 1991; Geldmacher et al., 2001; Geldmacher et al., in press).

Prior to this study, only a few geochronological or tracer isotope data were available for volcanoes emplaced

* Corresponding author. Fax: +33 4 92 07 68 16.
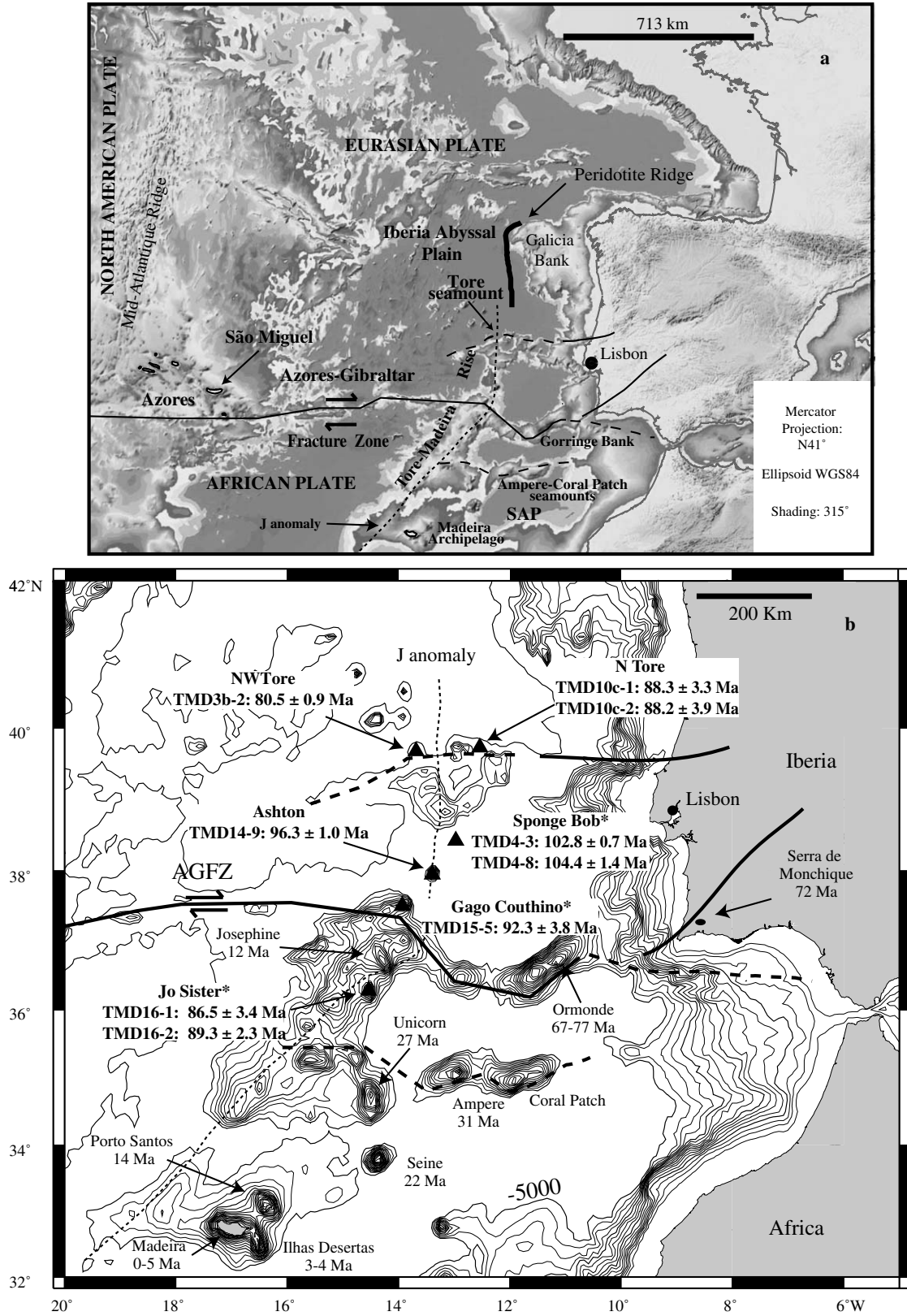 *E-mail address:* merle@chimie.univ-nantes.fr (R. Merle).

Fig. 1. (a) Map of the North Central Atlantic (modified after Sibuet et al., 2004a) distinguishing the main structural units. Solid lines represent faults, and dashed lines inferred faults. (b) Bathymetric map of the study region indicating the seamounts, sample locations and sample references. Seamount names for so far unnamed seamounts are marked (*). AGFZ, Azores-Gibraltar Fracture Zone. SAP, Seine Abyssal Plain. Ages of Ormonde, Monchique, Madeira, Porto Santo, Desertas Islands, Ampere, Josephine, Unicorn and Seine from Wendt et al. (1976); Féraud et al. (1981, 1982, 1986); Bernard-Griffiths et al. (1997); Schärer et al. (2000); Geldmacher et al. (2000, 2005). Location of the J anomaly after Olivet (1996).

between the Tore seamounts in the north, and Jo-Sister in the south (Fig. 1, Wendt et al., 1976; Geldmacher et al., in press). Rocks were collected by dredging during the 2001 "Tore-Madeira" cruise of the *Atalante*. Samples of kg-size were recovered, including basalts, trachy-andesites and trachytes with the latter two lithologies being as abundant as alkali basalts among the dredged rocks. The extent of seawater alteration is high in most rocks precluding systematic $^{40}Ar/^{39}Ar$ dating and isotope tracing of whole-rock samples. Given the strong degrees of alteration, only analyses of grain-by-grain selected mineral separates were possible, and as far as dating is concerned, the occurrence of primary magmatic titanite in most trachy-andesites and trachytes made it possible to use the U–Pb method. A few samples also contained very small amounts of zircon used for combined titanite–zircon dating and Hf isotope tracing on the same zircon grains. Fresh feldspar, either K-feldspar or plagioclase, was used for U–Pb (Pb–Pb) and Sr isotope analyses.

2. Geological framework

The Tore-Madeira Rise is a morphologically defined object. The Tore seamounts form a $\sim120 \times 90$ km wide elliptic complex at its northern end having summits reaching ~2500 m over the -5000 m deep Tore depression (Fig. 1). The southernmost seamount studied here is Jo Sister lying at ~500 km distance from the Tore locality. It culminates at about 4000 m above sea floor. Other seamounts investigated here are, from North to South, Sponge Bob, Ashton and Gago Couthino, reaching 3000 m, 3500 m, and 3200 m above the -5000 m deep seafloor, respectively (Fig. 1). Jo Sister has also been named Erik and Gago Couthino, Teresa (Hoernle et al., 2003; Geldmacher et al., in press) but none of these names has been ratified so far. An important structure is the Azores-Gibraltar Fracture Zone (AGFZ) which is an Atlantic transform fault separating the Eurasian and African plates. Its eastern end appears to split into three branches towards the Tore, Gorringe, and Ampere-Coral Patch seamounts (e.g., Laughton et al., 1975; Jiménez-Munt et al., 2001). Dextral strike-slip movements along this fracture zone seem to be absent or very small on the plate scale since the J anomaly is not visibly displaced (Fig. 1). Since Oligocene times, movements along the main branch and the branches to the North and South of the AGFZ seem to be transpressive, with a slight dextral component along the main fracture due to extension in the Azores region evidenced by the modeling of focal mechanisms (Olivet, 1996; Malod, personal commun.).

Volcanoes to the North of the AGFZ lie along the first Atlantic magnetic anomaly (J anomaly, 125–130 Ma) in this region. This anomaly corresponds to the boundary between true oceanic crust and a transitional domain being composed of rifted and stretched Iberian continental margin, unroofed lithospheric peridotites (e.g., peridotite ridge; Fig. 1) detached from lowermost continental crust (Boillot

et al., 1989; Beslier et al., 1993). This transitional zone has locally been intruded by syn-rift basaltic dikes and gabbros (Beslier et al., 1988; Boillot et al., 1995; Schärer et al., 1995, 2000). North to 41°30′N (Fig. 1), the J anomaly is not identified (south of Galicia Bank), implying that initial Atlantic opening along the Galicia Bank occurred later. To the South of the southern branch of the AGFZ, magnetic anomalies older than J seem to be present in the Seine Abyssal Plain (Roest et al., 1992) implying that some volcanoes to the South could be emplaced into oceanic lithosphere including the southern part of the Tore Madeira Rise.

Geophysical investigations show the rise substratum to be about 10 km thick, hypothetically containing some underplated magmas (Mauffret et al., 1989; Peirce and Barton, 1991; Pinheiro et al., 1992). It has also been suggested that formation of the rise represents a major event during opening of the Central and North Atlantic ocean (Olivet, 1996). This correlates with small-amplitude gravity anomalies suggesting that it is isostatically compensated on both the local and regional scale (Peirce and Barton, 1991).

A magmatic event distinct from ocean spreading is the emplacement of syn-rift related magmas prior or during the very early stages of Atlantic opening in the Iberia margin. Such gabbro and dolerite emplacement occurred at 121 Ma along the Galicia Bank (Féraud et al., 1988; Schärer et al., 1995, 2000) and at 138 Ma in the Gorringe Bank (Girardeau et al., 1998; Cornen et al., 1999; Schärer et al., 2000). These syn-rift subcontinental magmas have MORB source signatures and were most likely derived from the asthenosphere at that time.

Regionally important alkaline rocks, distinct from both syn-rift magmatism and 130–125 Ma Atlantic opening occur on the peridotitic–gabbroic Ormonde seamount, the Ampere-Coral Patch seamounts, as well as on the continent (Fig. 1). Rb–Sr, U–Pb and $^{40}Ar/^{39}Ar$ ages for these rocks range between 67–77 and 31 Ma (Rock, 1976; Féraud et al., 1982, 1986; McIntyre and Berger, 1982; Bernard-Griffiths et al., 1997; Geldmacher et al., 2000; Schärer et al., 2000). We will show that such alkaline magmatism is also a major component of the northern Tore-Madeira Rise, where differentiated alkaline rocks have been recognized.

3. Alkaline magmatism: previous studies

3.1. The Madeira archipelago

The 14 Ma to recent Madeira Archipelago is composed of volcanic and intrusive rocks of mostly alkaline affinity, where basalts range from tholeiites to basanites. $^{40}Ar/^{39}Ar$ ages on whole-rocks (total fusion) and plagioclase range from 4.63 ± 0.10 Ma to 0.18 ± 0.08 Ma (Geldmacher et al., 2000). The Desertas Islands of the archipelago are considered to be the N–S arm of the Madeira rift system for which $^{40}Ar/^{39}Ar$ whole-rock ages of basaltic lithologies range from 3.62 ± 0.24 to 3.25 ± 0.08 Ma (Geldmacher

et al., 2000). For Porto Santo Island located 45 km to the north-east of Madeira, alkali basalts to trachytic rocks (Geldmacher and Hoernle, 2000) have Ar whole-rock ages of 13.1 ± 0.4 and 12.3 ± 0.4 Ma (Féraud et al., 1981) and 14.31 ± 0.22 and 11.07 ± 0.10 Ma for plagioclase (Geldmacher et al., 2000). To explain source characteristics of Madeira volcanism contrasting hypothesis were proposed, (1) interaction of a high-$^{238}U/^{204}Pb$ (HIMU) plume component with N-MORB-like asthenosphere and oceanic lithosphere (Hoernle et al., 1991, 1995), (2) interaction of MORB source mantle with a mixture of HIMU and EMI-type mantle plume material (Mata et al., 1998), (3) recycling of relatively young oceanic crust (Thirlwall, 1997), (4) mixing of plume material containing a relatively young (~1.2 Ga) recycled oceanic crust and shallow MORB sources with a component of Paleozoic oceanic crust (Widom et al., 1999), (5) progressive melting of plume material containing relatively young (<1 Ga) recycled oceanic lithosphere from which enriched altered oceanic crust and depleted lower crust and lithospheric mantle were derived (Geldmacher and Hoernle, 2000, 2001), and (6) melting of metamorphosed oceanic lithosphere shortly after its formation (Halliday et al., 1992, 1993, 1995).

3.2. The Josephine, Seine, Unicorn, and Ampere-Coral Patch seamounts

Based on geochemical analyses and K–Ar whole-rock dating (12.6 ± 0.4 Ma; 8.2 ± 0.2 Ma) of the Josephine seamount it was originally suggested that the volcanoes building up the submarine mountain range between Josephine and the Tore localities reflect a Miocene magmatic event (Wendt et al., 1976). Further chemical analyses of Josephine lavas confirm its alkaline character (Merle et al., 2005).

Previous studies of three other volcanic complexes at Seine, Unicorn, and Ampere-Coral Patch (Fig. 1) yield whole-rock $^{40}Ar/^{39}Ar$ ages of 21.7 ± 0.2 Ma, 27.4 ± 2.4 Ma, and 31.20 ± 0.20 Ma, respectively (Geldmacher et al., 2000, 2005). It is important to note that they all lie significantly to the East of the Tore-Madeira Rise. The samples analyzed for these seamounts are olivine–phyric basanites and nephelinites with incompatible element characteristics similar to the volcanic rocks of the Madeira Archipelago. Initial Pb, Sr and Nd isotopic compositions of the Seine, Unicorn and Ampere-Coral Patch seamounts are interpreted as the result of interaction of Madeira plume melts with the overlying lithosphere, which contains continental lithospheric components (Geldmacher and Hoernle, 2000; Geldmacher et al., 2005).

3.3. The Ormonde seamount

This seamount marks the eastern summit of the Gorringe Bank. It is composed of peridotites that are intruded by 138 ± 1 and 136 ± 1 Ma old gabbros, and 67–77 Ma old alkaline lavas on top of the bank (Féraud

et al., 1982, 1986; Cornen, 1982; Cornen et al., 1999; Schärer et al., 2000). The alkaline lavas show two magmatic trends (1) highly alkalic, silica-undersaturated rocks, ranging from nephelinites to phonolites and (2) mildly alkaline, silica-saturated volcanics ranging from alkali basalt and basanites to trachytes (Cornen, 1982). The alkaline rocks from the Ormonde seamount are interpreted on the basis of initial Pb, Sr, Nd and Hf (on zircon) isotopic compositions to be derived from sub-lithospheric mantle melts (OIB-like source) contaminated by ancient Rb-depleted and LREE-enriched lithospheric mantle detached during passive continental rifting (Bernard-Griffiths et al., 1997; Schärer et al., 2000).

3.4. Continental Serra de Monchique

This complex (Fig. 1) is a sub-volcanic nepheline syenite body interpreted as belonging to the Late Cretaceous Iberian Alkaline Igneous Province, related to late stages of opening of the Bay of Biscay (McIntyre, 1977; Cornen, 1982; McIntyre and Berger, 1982; Rock, 1982; Whitmarsh et al., 1986). Dominant lithologies are nepheline syenites and micro-syenites with minor gabbros and lamprophyres, having incompatible elements patterns similar to the alkali lavas on the Ormonde seamount. These rocks do not exhibit any chemical or isotope signatures for the assimilation of continental crust (Bernard-Griffiths et al., 1997). A whole rock-mineral Rb–Sr age for Serra de Monchique, and K–Ar mineral measurements yield an age of 72 ± 2 Ma (Rock, 1976; McIntyre and Berger, 1982; Bernard-Griffiths et al., 1997). Similar model for magma genesis are proposed for Ormonde and Monchique (Bernard-Griffiths et al., 1997).

4. Samples descriptions

4.1. Overview

Samples collected during the "Tore-Madeira Rise" cruise represent 40 different dredge sites located along the flanks of the different seamounts. Magmatic rocks were recovered in 22 dredges with exclusively basaltic lithologies to the south of the Jo-Sister locality, and significantly differentiated lithologies to the north (Fig. 1). Individual dredge depth of our samples are given in Table 1, ranging from -5007 to -1560 m representing seamount flank sections between about 1 and 6 km, taking into account individual seamount slopes measured at the sample localities. Although the depth of sections are different among the seamounts, the sampled rocks cover basal sections, intermediate levels, and top sections of the 3000–4000 m high seamounts. We therefore consider that sampling is representative for lithologies constituting the different seamounts, even if not all mounts could be sampled from the bottom to the top.

Since most magmatic rocks have suffered significant low-temperature alteration by seawater, dating accessory minerals by the U–Pb chronometers was potentially the

Table 1
Petrological and mineralogical descriptions of rock samples from the different seamounts

Samples	Location	Dredging depth (m) max–min	Rock type	Alteration (%)	Texture	Phenocrystals	Groundmass
Tore Smt (NW) TMD3b-2	39°41.66N, 13°41.66W	4930–3350	Trachyte	5–10	Almost aphyric, micro-vesicular, microlitic fluidal	Rare mm-size An_{37} to anorth (An_6; Or_{21}), diop (micro-phenocrysts): $Wo_{47–49}$; $En_{27–30}$; $Fs_{23–24}$, Fe–Ti ox	Lath of Anorth ($An_{7–9}$; $Or_{19–23}$), pyroxene, Fe–Ti ox
Tore Smt (N) TMDIOc-1	39°45.33N, 12°23.36W	5007–4589	Trachy-andesite	10–15	Slightly porphyritic, micro-vesicular, microlitic fluidal	Plag $An_{40–44}$, Mg-hasting, diop (rare) $Wo_{48–49}$; $En_{29–33}$; $Fs_{19–22}$	Feldspar lath, Fe–Ti ox, diop, Mg-hasting (sparse)
TMD10c-2			Trachy-andesite	15	Slightly porphyritic, micro-vesicular, microlitic fluidal	Plag (oscillatory zoned) $An_{38–47}$, microphenocrysts of Mg-hasting (minor), diop $Wo_{46–48}$; $En_{27–30}$; $Fs_{21–27}$, titanite (very rare)	Laths of plag $An_{18–41}$, Fe–Ti ox, diop, Mg-hasting (rare)
Sponge Bob Smt TMD4-3	38°27.50N, 12°54.00W	3811–3243	Trachyte	5	Slightly porphyritic, microlithic fluidal	3–4mm-size euhedral sanidine $Or_{36–42}$; $Ab_{56–62}$ (sparse), biotite, titanite, Fe–Ti ox	Feldspar laths, Fe–Ti ox, patchy biotite
TMD4-8			Trachyte	5–10	Porphyritic, microlithic fluidal	3–4 mm-size euhedral K-feld $An_{1–8}$; $Or_{25–48}$ ($\approx$3% modal), biotite, titanite, Fe–Ti ox (microphenocrysts)	Feldspar laths, Fe–Ti ox, patchy biotite
Ashton Smt TMD14-9	38°01.54N, 13°22.66W	2803–2395	Trachyte	<5	Highly porphyritic, microlithic fluidal	6 mm–10 mm-size zoned K-fsp $An_{2–11}$; $Or_{18–40}$ ($\approx$5% modal), subordinate mm-size biotites, diop $Wo_{45–46}$; $En_{38–39}$; $Fs_{15–16}$ (sparse), Fe–Ti ox, apatite	Feldspar lath, Fe–Ti ox, biotite, needles of pyroxene
Gago Coutinho Smt TMD15-5	37°30.64N, 13°55.46W	2846–1560	Trachyte	5–10	Almost aphyric, microlithic fluidal	Euhedral zoned feldspar: An_6 to anorth (An_6; Or_{34}), Mg-hasting, diop $Wo_{45–46}$; $En_{31–32}$; $Fs_{22–23}$ (minor), Fe–Ti ox, titanite	Lath of anorth ($An_{8–9}$; $Or_{18–20}$), Fe–Ti ox, pyroxene
Jo-Sister Smt TMD16-1	36°21.33N, 14°26.84W	2224–1960	Trachy-andesite	35	Almost aphyric, microlithic fluidal	Clino-amphibole (hastingsite, kaersutite), core-altered plag $An_{55–58}$ (rare), titanite, Fe–Ti Ox	K-fsp laths ($Or_{22–46}$; $An_{2–15}$), Fe–Ti ox
TMD16-2			Trachy-phonolite	25	Almost aphyric, microlithic fluidal	Clino-amphibole (hastingsite, kaersutite), diop $Wo_{47–49}$; $En_{29–38}$; $Fs_{13–24}$ (microphenocrysts), titanite, Fe–Ti ox	K-fsp laths ($Or_{22–46}$; $An_{2–15}$), Fe–Ti ox

An, anorthite; Or, orthoclase; anorth, anorthoclase; diop, diopside; ox, oxides; Mg-hasting, magnesio-hastingsite; plag, plagioclase; K-fsp, K-feldspar. Microprobe analyses (EPMA) were performed with a Cameca instrument (Microsonde Ouest, Brest). Analytical conditions were 15 kV, 15 nA, counting time 6 s, and correction by the ZAF method. Concentrations of <0.3% are considered qualitative.

most promising method to avoid alteration-induced bias on the ages. Seawater alteration partly transformed the crypto-crystalline groundmass to clay minerals, and facilitated Fe–Mn hydroxide in-filling of cracks and vesicles. In examining all differentiated rocks, only 5 trachytes and 4 trachy-andesites contained primary magmatic titanite and in consequence, our investigation was limited to these samples representing six seamounts (Fig. 1). Zircon was recovered from three of the titanite-bearing alkaline volcanics allowing combined U–Pb zircon–titanite dating and Hf isotope measurements on zircon.

4.2. Detailed sample description

The principal petrographical and mineralogical characteristics of the samples (thin sections and Electron Probe Microanalyses) are given in Table 1. The groundmasses of these samples show microlitic fluidal textures consisting of laths of feldspars. A trachyte (TMD3b-2, 0.5 kg in weight) dredged at NW-Tore is almost aphyric, displaying rare mm-size feldspar phenocrysts, euhedral titanites and few zircons. The matrix underwent alteration characterized by Fe–Mn hydroxides lining the inner walls of vesicles. The two samples from the northern part of Tore seamount (TMD10c-1; TMD10c-2, 1.4 and 0.2 kg in weight, respectively) are trachy-andesites, being slightly plagioclase-phyric and carrying sparse brown amphiboles. Alteration is characterized by Fe–Mn hydroxides, coating inner walls of vesicles. Titanite is less abundant in TMD10c-2 than in TMD10c-1 and no zircon could be seen.

The two Sponge Bob trachyte samples (TMD4-3, 1 kg in weight; TMD4-8, 2.5 kg in weight) are porphyritic in mm-size K-feldspar phenocrysts containing abundant titanite. TMD4-3 contains also a few zircons. The Ashton sample (TMD14-9, 1 kg in weight) is a fresh highly porphyritic trachyte yielding abundant titanite and large zircons reaching more than 1 mm in length. Zircon and titanite contain frequent inclusions of apatite and oxides. The trachyte dredged on the Gago Coutinho seamount (TMD15-5, 1 kg in weight) is almost aphyric containing rare euhedral phenocrysts of zoned feldspars. Alteration is characterized by Fe–Mn hydroxides along cracks. Titanite is abundant and typically contains oxide inclusions; but zircon was absent.

The trachy-andesite samples from the Jo Sister seamount (TMD16-1; TMD16-2, 4 and 1.5 kg in weight respectively) are the most altered of all our samples. Borders of all TMD16-1 fragments are yellow-orange colored, due to palagonization of the groundmass, whereas the interior is light grey. Sample TMD16-2 contains rare hastingsite–kaersutite phenocryst and abundant grains of titanite but no zircon. Alteration phases are hydroxides and clay minerals partly replacing the groundmass.

Fifty-four abraded and non-abraded titanite and 10 zircon fractions were selected from nine different trachy-andesites and trachytes for U–Pb geochronology. To search for heterogeneities, overgrowths, and inclusions, all populations were examined by optical microscopy, back-scattered

electrons (BSE), and cathodoluminescence (CL) as displayed in Fig. 2. Grain-by-grain selection of the essentially transparent titanites and zircons covers the full range of habits constituting the populations (Figs. 2a–e). Titanites are pale to dark yellow and occasionally light brown reflecting pleochroism. Opaque inclusions are abundant and most fractions analyzed contained such inclusions (Figs. 2f, g and i), as well as some transparent colorless euhedral crystals (probably apatites). Zircons are colorless and also contain transparent and opaque inclusions (Figs. 2d and e). No significant growth heterogeneities, overgrowth or old cores could be detected.

5. Analytical procedures

Mineral separation was carried out using Franz isodynamic magnetic separator, heavy liquids (CHBr$_3$ and CH$_2$I$_2$), and grain-by-grain hand-picking under the binocular microscope. Major and trace element analyses were carried out by ICP-AES and ICP-MS at the University of Brest (analytical procedures in Cotten et al., 1995) and the CRPG at Nancy (analytical procedures in Govindaraju and Mevelle, 1987 and Carignan et al., 2001). U–Pb and Pb isotope measurements were performed on a Thomson 206 mass-spectrometer using a SEM for U–Pb analyses, and a Faraday cage for Pb. Sr composition measurements were made on the VG-Sector mass-spectrometer. Lead and U isotopic ratios were corrected for $0.10 \pm 0.05\%$/amu of mass-fractionation on the SEM, as determined from repeated runs of a mixed NBS-981 Pb/NBS-960 U standard, as well as the gravimetrically calibrated ^{233}U/^{235}U spike (NBS-995/NBS-993). For NBS-981 Pb our mean ratios ($n = 8$) corrected for mass-discrimination are: 16.941 ± 0.004 (2-sigma-STERR) for ^{206}Pb/^{204}Pb, 15.501 ± 0.004 for ^{207}Pb/^{204}Pb, and 36.728 ± 0.009 for ^{208}Pb/^{204}Pb. For Faraday measurements, mass-fractionation on Pb is $0.10 \pm 0.03\%$/amu. Repeated measurements of total Pb blanks (2004–2005) yielded $60 \pm 30\%$ pg for titanite and $20 \pm 60\%$ pg for zircon, with less than 1 pg blank U for both procedures. Zircon and titanite grains were mechanically abraded to eliminate potentially altered crystal surfaces (Krogh, 1982). Prior to dissolution in pure >50% HF, titanite, zircon, and plagiclase were spiked with a mixed ^{205}Pb/^{235}U solution, whereas K-feldspar, devoid of U, was measured for composition only. Zircons were dissolved at 215 °C for 3 days in Teflon bombs followed by anion exchange chemistry (modified from Krogh, 1973). Titanite and feldspar was dissolved in PFA Teflon beakers at 180 °C (~18 h). An HBr procedure was used, for separation and purification of U and Pb from titanite and plagioclase, modified after Manhès et al. (1978). For U–Pb, Pb and Sr analyses, grain-by-grain selected feldspars were washed in HCl 6 N, ground in an agate mortar, and leached with 1% HF/HBr 1 N for a few minutes in the ultrasonic bath (e.g., Schärer, 1991) prior to dissolution.

Strontium composition measurements on size-fractions of grain-by-grain selected feldspars were done on unspiked
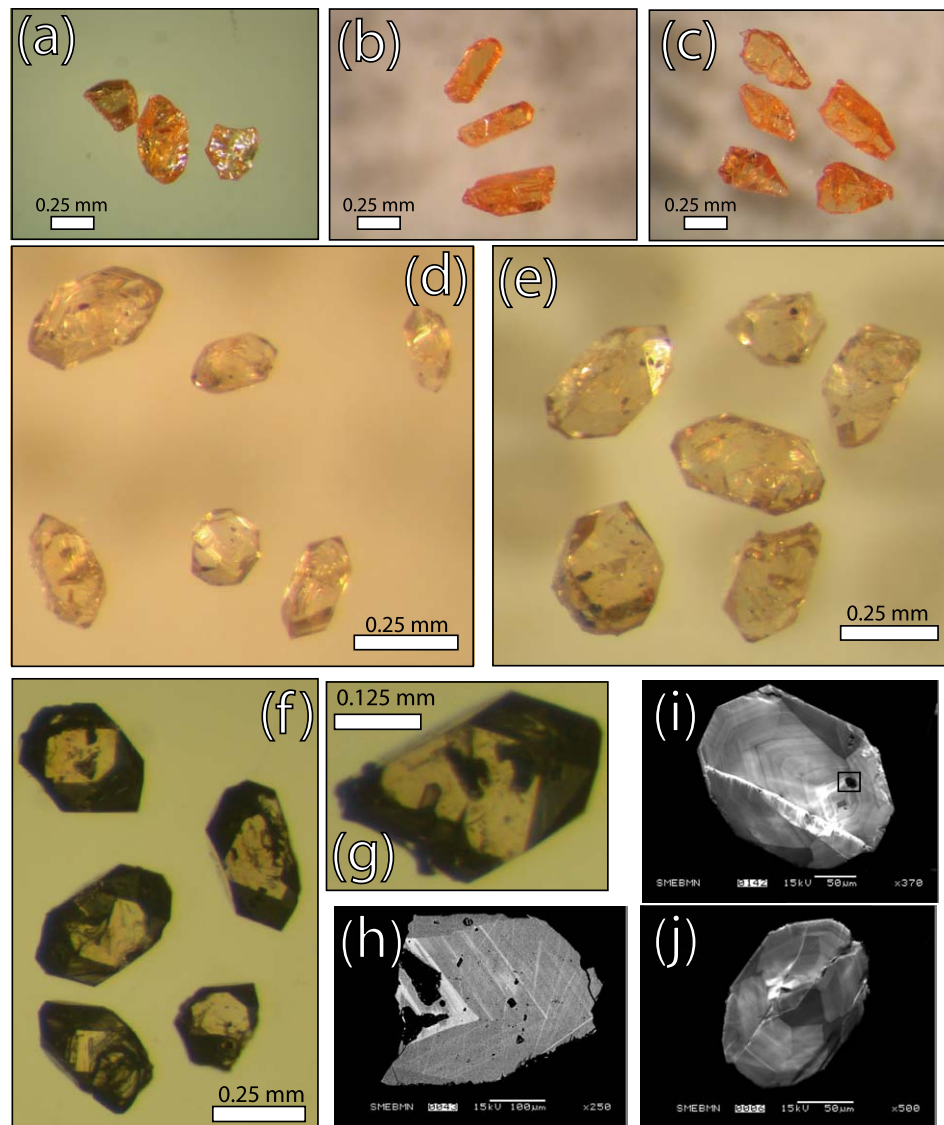
Fig. 2. Photomicrographs, CL and BSE images illustrating titanite and zircon grains. (a) prismatic fragments and a euhedral crystal of titanite; (b) and (c) two different types of euhedral crystals of titanites; (d) and (e) zircons with opaque and transparent inclusions; (f) (transmitted light) zircon with transparent inclusions; (g) zircon grain showing a well crystallized transparent inclusion, probably an apatite; (h) BSE image of a polished titanite grain showing regular oscillatory growth zoning; (i) cathodoluminescence (CL) image of a polished zircon grain showing well-developed regular oscillatory zoning, a well-crystallized inclusion is outlined; (j) CL image of a polished zircon grain showing well-developed regular oscillatory zoning.

aliquots on 2/3 of the total sample solution, reserving 1/3 of the parent solution for spiking with a mixed $^{85}Rb/^{84}Sr$ tracer for Rb–Sr concentration determination. For Sr chemical separation, we employed Eichrom Sr-Spec. resin while Rb separation was done with the AGW50-X12 cation resin. Sr measurement accuracy was monitored using NBS-987 standard yielding a mean ($n = 8$) ratio of 0.71026 ± 0.00005 (2-sigma-STERR). Hafnium isotope measurements were performed on the Plasma-54 instrument at the Ecole Normale Supérieure at Lyon using the JMC-475 Hf standard for calibration after each sample (Blichert-Toft et al., 1997). All data were normalized to $^{176}Hf/^{177}Hf = 0.282161$ based on replicate analyses of JMC 475, run before and after each analysis. For Hf isotope analyses, the 3 N HCl fraction from the U–Pb proce-

dure was treated on the AGW50-X8 resin to avoid interferences from ^{176}Yb (e.g. Patchett and Tatsumoto, 1980; Bodet and Schärer, 2000). Isochrons were calculated after Minster et al. (1979) and Ludwig (2003) with the latter also used for constructing concordia plots.

6. Major and trace element results

6.1. Major elements

Compositions range in SiO_2 from 56 to 63 wt% and between 0.21 and 0.67 wt% for MgO (Table 2), being consistent with trachy-andesites to trachytes. The wide range of alteration is reflected by their Loss On Ignition (LOI: 0.58–8.36 wt%). In the total-alkali vs. SiO_2 diagram

Table 2
Major and trace element analytical results of rock samples from the different seamounts

Sample:	TMD3b-2	TMD10c-1	TMD10c-2	TMD4-3	TMD4-8	TMD14-9	TMD15-5	TMD16-1	TMD16-2
Seamount:	Tore (NW)	Tore (N)	Tore (N)	Sponge Bob	Sponge Bob	Ashton	Gago Coutinho	Jo Sister	Jo Sister
SiO_2 (wt%)	62.00	58.18	58.45	62.98	63.40	60.25	62.20	56.40	56.67
TiO_2	0.38	0.70	0.71	0.35	0.48	0.60	0.26	0.43	0.39
Al_2O_3	18.75	19.64	19.30	18.06	18.60	17.84	19.35	19.55	18.25
Fe_2O_3*	2.86	3.94	3.87	2.33	2.11	2.53	2.08	3.10	2.96
MnO	0.23	0.22	0.29	0.10	0.06	0.11	0.12	0.28	0.20
MgO	0.38	0.59	0.58	0.31	0.21	0.41	0.28	0.67	0.55
CaO	2.43	2.69	2.65	0.39	0.35	3.66	1.09	0.93	2.11
Na_2O	6.75	6.18	6.20	6.61	6.45	6.10	6.75	4.95	5.37
K_2O	4.60	4.10	3.85	5.59	6.85	5.91	5.30	5.15	6.55
P_2O_5	0.08	0.19	0.11	0.09	0.06	0.53	0.03	0.06	0.67
LOI	1.07	3.54	4.00	3.07	1.29	1.99	2.44	8.36	6.19
Total	99.53	99.97	100.02	99.88	99.86	99.93	99.90	99.88	99.90
Na_2O+K_2O	11.35	10.28	10.05	12.20	13.30	12.01	12.05	10.10	11.92
Q	0.05	—	—	1.89	—	—	—	4.21	—
Cor	—	0.62	0.40	0.66	0.08	—	0.62	4.69	0.10
Ne	—	—	—	—	1.34	3.12	—	—	4.10
Rb (ppm)	76.0	60.7	43.5	211.0	185.0	105.0	105.0	62.0	105.0
Sr	692	862	835	26	63	377	392	98	338
Ba	1200.0	987.0	1025.0	14.3	240.0	643.0	0240.0	265.0	240.0
V	19	18	20	36	32	19	12	15	15
Cr	5.5	—	2.0	—	4.0	—	2.5	2.0	—
Co	1.5	1.2	1.0	0.4	0.8	1.6	21.0	1.0	1.9
Ni	11.0	24.6	37.0	—	2.5	5.5	10.0	53.0	31.3
Y	11.0	22.5	12.8	86.8	57.0	31.2	5.2	20.5	25.0
Zr	355	387	502	1007	1235	637	262	955	899
Nb	81	114	122	173	261	129	48	227	188
La	97	59	39	187	180	110	33	117	112
Ce	213	186	190	283	290	182	136	213	183
Nd	40.0	50.1	30.5	106.0	72.0	68.1	18.0	50.0	46.0
Sm	5.10	8.09	5.15	16.20	9.60	11.00	2.10	6.65	6.28
Eu	1.55	2.94	2.12	3.30	2.18	2.76	0.74	1.43	1.19
Gd	3.10	6.20	3.85	12.80	8.50	7.16	1.40	4.80	4.32
Dy	2.10	4.68	2.85	13.80	8.20	6.84	0.90	3.95	4.49
Er	1.10	2.06	1.30	9.52	5.80	3.11	0.50	2.20	2.50
Yb	1.09	1.69	1.14	16.60	6.40	3.64	0.47	2.10	2.97
Th	13.7	13.8	13.2	49.5	29.0	14.1	19.3	29.0	25.4
Eu/Eu*	1.19	1.27	1.46	0.70	0.74	0.95	1.32	0.77	0.70

Major and trace elements of samples TMD 3b-2, TMD4-8, TMD10c-2, TMD15-5 and TMD16-1 were obtained by ICP-AES at Brest (Université de Bretagne Occidentale) following the method described in Cotten et al. (1995). Relative standard deviations are <2% for major elements, Rb and Sr, and <5% for other trace elements. Analyses of samples TMD4-3, TMD10c-1, TMD14-9 and TMD16-2 were performed at Nancy (CRPG-CNRS). Major elements were obtained by ICP-AES following the method described in Govindaraju and Mevelle (1987) and trace elements by ICP-MS following the method in Carignan et al. (2001). Analytical precision is at 1–5% for major elements, except for MnO, MgO, Ca$_2$O and P$_2$O$_5$ (10%). For trace elements, analytical precision is in the range 5–10% for abundances >50 ppm, 5–15% between 50 and 10 ppm, 5–20% between 10 and 1 ppm and 5–25% for abundances <1 ppm. Fe$_2$O$_3$*, total iron expressed as Fe$_2$O$_3$. LOI, loss on ignition. Eu/Eu* = Eu$_N$/$\sqrt{(Sm_N \times Gd_N)}$. CIPW norms calculated with adjusting Fe^{3+}/Fe^{2+} ratio after Middlemost (1989). Q, normative quartz; Cor, normative corundum; Ne, normative nepheline.

(Fig. 3; TAS, Le Bas et al., 1986), all rocks lie either in the trachyte or trachy-andesite fields corroborating their alkaline affinity. One rock (TMD16-2) plots in the tephri-phonolite field. This classification has to be considered to be influenced by the high degrees of seawater alteration. The freshest rocks are trachytes having less than 2 wt% of LOI, being devoid of CIPW normative corundum (Table 2, TMD3b-2; TMD4-8; TMD14-9). They are moderately alkaline (Na$_2$O + K$_2$O: 10–13 wt%), sodi-potassic, and slightly under-saturated or saturated in SiO$_2$ such as observed for trachytes on the Ormonde seamount (Bernard-Griffiths et al., 1997), where alkali magmatism was dated at 67–77 Ma (Féraud et al., 1982, 1986; Schärer et al.,

2000). The other rocks contain CIPW normative corundum (<5 wt%), associated in two rocks with significant CIPW normative quartz, which most likely is the direct result of seawater alteration.

6.2. Trace elements

Compatible trace element contents are low (Table 2; Ni < 53 ppm, Cr < 5.5 ppm, Co < 21 ppm, V < 36 ppm) which is in agreement with values expected for evolved lavas (Table 2). Cobalt content in the Gago Coutinho sample (TMD15-5) is high with respect to the other samples where compatible elements contents are low. This feature could
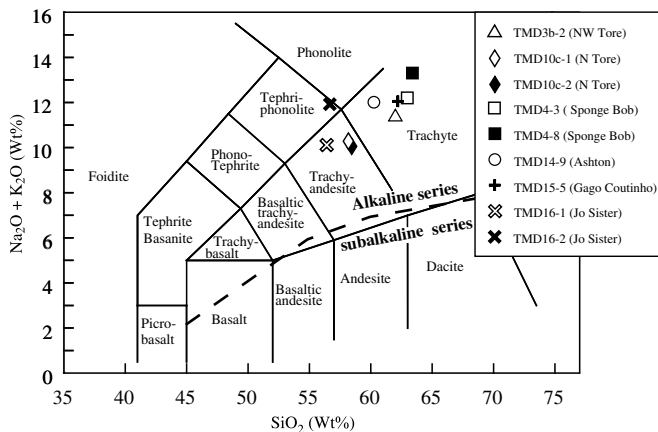
Fig. 3. Total-alkali vs. silica (Le Bas et al., 1986) discrimination diagram for our samples. The thick dashed line represents the boundary between the alkaline and the sub-alkaline domains (Miyashiro, 1978).

be related to seawater alteration of Fe–Mn hydroxides that incorporated Co. The incompatible element patterns of our samples (Fig. 4) are very similar to these of trachytes from Ormonde and Madeira which are interpreted to be produced by fractional crystallization from basaltic parental melts.

Five samples show negative anomalies in Sr and Ba (TMD4-3, TMD4-8, TMD14-9, TMD16-1 and TMD16-2). Although these rocks underwent various degrees of alteration the amplitude of trace element abundances do not seem to be correlated with alteration; they seem to be partly magmatic. Slightly negative Eu anomalies (Fig. 5) suggest fractionation of sodi-potassic feldspars during late stages of crystallization (Villemant et al., 1980). Rocks without Sr and Ba anomalies show weak positive Eu anomalies indicating that plagioclase is a cumulate phase in these rocks.

The concave shape of REE patterns is consistent with removal of amphibole and apatite from the magma (Fig. 5). The trachyte from Gago Coutinho (TMD15-5) displays significant depletion in moderately and slightly incompatible elements relative to trachytes from the Madeira Archipelago and Ormonde trachytes (Figs. 4 and 5). This suggests very evolved stages of crystallization including apatite fractionation causing magma depleted in middle REE and Y, and titanite producing depletion in middle REE and Nb. Fractionation of the latter phase is evidenced by Nb depletion. Such depletion also occurred in the TMD3b-2 lava (Tore NW). Three samples display Ce anomalies that could be related to the filling of vesicles and cracks by Fe–Mn hydroxides.

7. Geochronological and isotope results

7.1. General

The Tables 3 and 4 lists U–Pb analytical results of titanites and zircons, Table 5 gives initial Pb composition of

feldspars, Table 6 lists Rb–Sr analytical results for feldspars, and Table 7 shows initial Hf isotope compositions of zircon. For more analytical details we refer to the corresponding footnotes. Concordia and isochron diagrams for U–Pb analytical results are given in the Figs. 6–8. Initial Pb isotopic composition of feldspars are shown in Fig. 9, relative to the evolution of continental crust, the MORB-type mantle, and isotope signatures measured in magmatic rocks related to seamount formation in the Central Atlantic region (Fig. 10).

Given the fact that all titanites from the seamounts have significant amounts of initial common Pb, relative to radiogenic Pb, data are presented in both the Concordia ($^{207}Pb/^{235}U$ vs. $^{206}Pb/^{238}U$) and isochron diagrams ($^{238}U/^{204}Pb$ vs. $^{206}Pb/^{204}Pb$). The fundamental difference with this approach is that data of the Concordia plot are corrected for initial Pb, whereas the isochron data include initial Pb reflecting two different ways to derive ages. Since the titanite populations are young and poor in U, and consequently poor in radiogenic Pb, all ages are based on the $^{206}Pb/^{238}U$ chronometer because $^{207}Pb/^{235}U$ is not precise enough; however, the latter ratios serve to test whether the U–Pb chronometer behaved within analytical limits as a closed system since crystallization. Some of the ellipses (e.g., Figs. 6e and 8a) plot slightly to the left of the concordia curve, which can be explained by the uncertainty in common Pb correction due to real differences of intial Pb compositions in titanite, not identical to that measured in cogenetic feldspars.

7.2. U–Pb dating

7.2.1. Tore seamounts

From the northernmost expression of the volcanic range at Tore (Fig. 1) two samples were analyzed for titanite, and a third rock for titanite and zircon. In all populations, crystal surfaces are well developed and devoid of any corrosion features. From the TMD3b-2 trachyte from NW Tore, a series of 5 abraded and unabraded titanite and 4 zircon size fractions were analyzed. Titanites yield identically concordant data (Fig. 6a), defining an average $^{206}Pb/^{238}U$ age of 80.5 ± 0.9 Ma (2σ STERR). The same data produce together with initial Pb of cogenetic plagioclase an isochron age of 82.1 ± 2.4 Ma (Fig. 6b). The four zircon fractions yield one concordant and 2 very slightly discordant fractions with $^{206}Pb/^{238}U$ ages within error of the titanites. The fourth fraction plots about 10% discordant yielding a slightly older age around 99 Ma. These dates were not included in age calculation.

Six titanite fractions from the trachy-andesite (TMD10c-1) from north Tore yield identically concordant and very slightly discordant data defining a mean $^{206}Pb/^{238}U$ age of 88.3 ± 3.3 Ma (Fig. 6c). Plotted together with Pb data from plagioclase they yield a $^{238}U/^{204}Pb$ vs. $^{206}Pb/^{204}Pb$ isochron age of 87.8 ± 1.6 Ma (Fig. 6d). The third sample (TMD10c-2) is also a trachy-andesite from the same locality, for which four titanite fractions yield 3
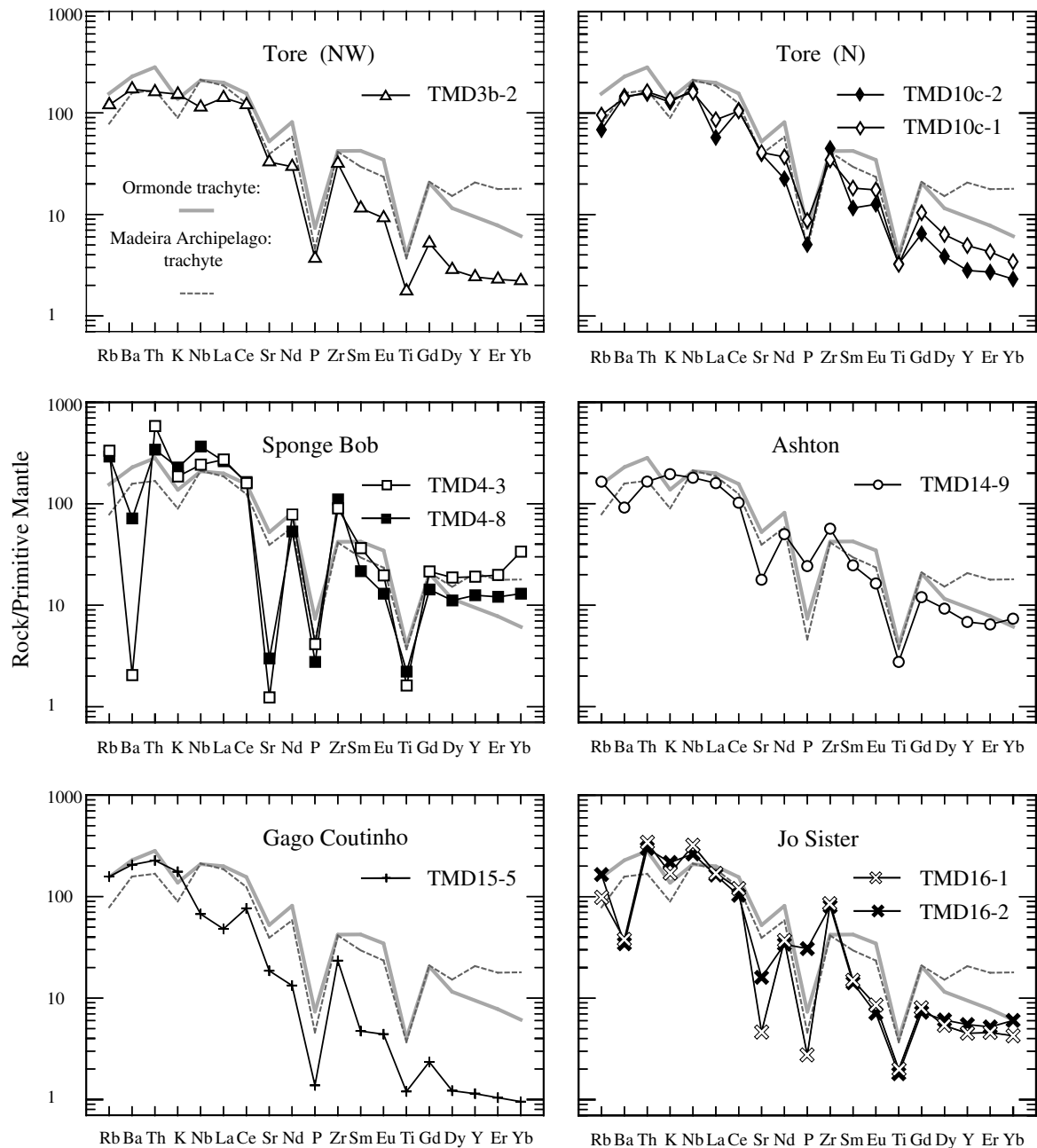
Fig. 4. Primitive mantle-normalized trace element patterns of the trachy-andesitic to trachytic samples studied here. For comparison are given a trachyte from the Ormonde seamount (Bernard-Griffiths et al., 1997) and a trachyte from the late Miocene-Quaternary Madeira Archipelago (Geldmacher and Hoernle, 2000). Normalization values from Sun and McDonough (1989).

identically concordant dates and a slightly discordant fraction defining together a mean age of 88.3 ± 3.9 Ma (Fig. 6e). Regressed with initial Pb of plagioclase they yield a $^{238}U/^{204}Pb$– $^{206}Pb/^{204}Pb$ isochron age of 88.0 ± 4.5 Ma (Fig. 6f).

7.2.2. Sponge Bob seamount

Six titanite size-fractions from the Sponge Bob trachyte TMD4-3 yield identically concordant ages defining a mean age of 102.8 ± 0.7 Ma (Fig. 7a) and 3 zircon fractions give concordant to slightly discordant dates, with two fractions within error of the mean titanite age. The most discordant

fraction yields a slightly older age of about 111 Ma. Regressed together with K-fsp. the 6 titanite fractions give a isochron age of 102.7 ± 0.7 Ma (Fig. 7b). Six titanite fractions from the other trachyte (TMD4-8) yield equally concordant data defining a mean titanite age of 104.4 ± 1.4 Ma in the concordia plot (Fig. 7c) and 107.2 ± 3.4 Ma together with K-fsp. in the $^{238}U/^{204}Pb$–$^{206}Pb/^{204}Pb$ isochron treatment (Fig. 7d).

7.2.3. Ashton seamount

Eight size-fractions of titanite from a trachyte (TMD 14-9) plot identically concordant defining an mean age of
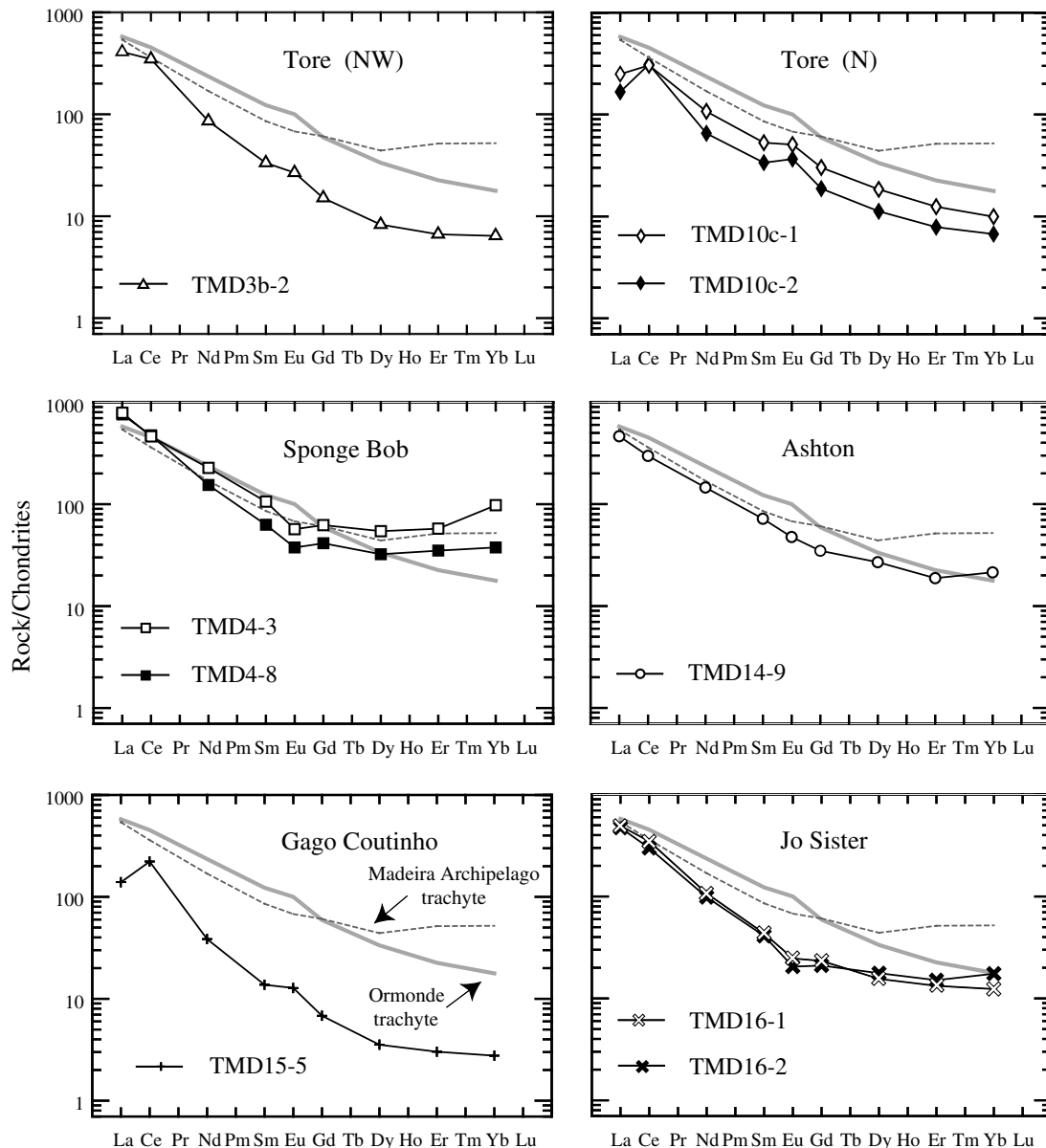
Fig. 5. Chondrite-normalized REE patterns of the samples studied here including the two reference rocks from Ormonde and Madeira seamount complexes. Normalization values from Sun and McDonough (1989).

94.3 ± 2.4 Ma, and two zircon fractions plot equally concordant (Fig. 7e). A third zircon analysis is about 2% discordant. The mean $^{206}Pb/^{238}U$ age of 96.8 ± 1.1 Ma for the three zircon fractions is identical to the titanite age. The full set of titanite and zircon data yields a mean age of 96.3 ± 1.0 Ma. The eight titanite fractions define together with K-fsp. a $^{238}U/^{204}Pb$–$^{206}Pb/^{204}Pb$ isochron age of 93.7 ± 0.7 Ma (Fig. 7f).

7.2.4. Gago Coutinho seamount

Two of the five titanite fractions from a trachyte (TDM15-5) yield identically concordant ages, whereas the other three analyses plot by 2–4% discordant having slightly older $^{207}Pb/^{235}U$ ages (Fig. 8a). The mean $^{206}Pb/^{238}U$ age of all fractions is 92.3 ± 3.8 Ma. Their $^{238}U/^{204}Pb$–$^{206}Pb/^{204}Pb$

isochron age including K-fsp. is 93.8 ± 1.5 Ma (Fig. 8b). These titanite ages agree within error with two new hornblende ages from other rocks of this seamount yielding 92.9 ± 0.6 and 94.5 ± 0.4 Ma obtained by the $^{40}Ar/^{39}Ar$ method (Geldmacher et al., in press).

7.2.5. Jo Sister seamount

Four titanite fractions from the trachy-andesite TMD16-1 plot identically concordant, whereas a fifth fraction lies about 2% discordant (Fig. 8c). Their mean $^{206}Pb/^{238}U$ age is 86.5 ± 3.4 Ma. All fractions regressed together with initial Pb measured in K-fsp. yield an isochron age of 86.7 ± 0.9 Ma (Fig. 8d). The tephri-phonolite sample (TMD16-2) yielded eight identically concordant titanite analyses, and a slightly discordant data defining a

Table 3
U–Pb analytical results (Concordia plot) for titanites and zircons from the different seamounts

Sample description[a]	Weight (mg)	Concentration (ppm)		$\frac{^{206}Pb}{^{204}Pb}$	Radiogenic Pb in atomic %[c]			Atomic ratios[c]				Apparent ages Ma[c]		Corr. Coef.
		U	Pb rad.	Meas.[b]	^{206}Pb	^{207}Pb	^{208}Pb	$\frac{^{206}Pb}{^{238}U}$	%err (2σ)	$\frac{^{207}Pb}{^{235}U}$	%err (2σ)	$\frac{^{206}Pb}{^{238}U}$	$\frac{^{207}Pb}{^{235}U}$	
TMD 3b-2 (NW Tore)														
Titanite														
(1) Titanite ≈25 gr., NA, Ss, Pr. Frag., Gdn. to Lgt. Yw, opaq. incl.	0.2651	13.69	0.38	36.16	37.8	1.6	60.6	0.01222	8.5	0.0712	35.0	78.3	69.8	0.40
(2) Titanite 3 gr., Ls, sPr., Lgt, Yw, opaq. incl.	0.2990	13.66	0.44	44.10	35.8	2.1	62.1	0.01332	6.8	0.1073	16.3	85.3	103.5	0.51
(3) Titanite 12 gr., Ls, sPr., Lgt. Yw, opaq. incl.	0.3210	14.93	0.45	44.25	36.6	1.9	61.5	0.01263	7.5	0.0893	17.0	80.9	86.9	0.53
(4) Titanite 5 gr., Ls, sPr., Lgt. Yw	0.3455	15.61	0.48	50.48	36.3	2.1	61.6	0.01284	5.7	0.1003	14.1	82.3	97.1	0.51
(5) Titanite 6 gr., Ls, sPr., Lgt. Yw, opaq. incl.	0.2484	14.98	0.44	56.64	37.6	4.9	60.5	0.01275	9.9	0.0896	12.0	81.7	87.1	0.82
Zircon														
(6) Zircon 5 gr., Ss, sPr., Dk to Pl. Yw,	0.0900	117.29	2.01	135.54	62.7	3.0	34.3	0.01249	1.9	0.0832	4.2	80.0	81.2	0.54
(7) Zircon ≈15 gr., Ss, sPr., Pl. Yw	0.0426	197.41	3.08	146.17	68.6	3.5	27.9	0.01242	2.4	0.0871	3.5	79.5	84.8	0.72
(8) Zircon ≈12 gr., Ss, sPr., Pl. Yw	0.0787	232.75	4.66	305.98	54.7	2.9	42.4	0.01268	2.1	0.0932	4.2	81.2	90.5	0.58
(9) Zircon ≈10 gr., Ss, sPr., opaq. incl.	0.0430	394.71	7.42	452.49	71.0	3.8	25.2	0.01549	1.3	0.1131	2.8	99.1	108.8	0.54
TMD 10c-1 (N Tore)														
Titanite														
(10) Titanite 8 gr., Ms to Ls, sPr., Gd. to Lgt. Yw, opaq. incl.	0.2286	9.59	0.30	30.65	37.0	2.0	61.0	0.01326	9.5	0.0975	38.9	84.9	94.5	0.44
(11) Titanite 4 gr., Ls to VLs, sPr., Gdn. Yw	0.3191	9.75	0.34	48.98	34.6	2.1	63.3	0.01396	9.8	0.1162	17.4	89.4	111.6	0.62
(12) Titanite 14 gr., Ss to Ms, sPr., Gdn. Yw, opaq. incl.	0.2793	9.82	0.34	48.00	33.8	2.0	64.2	0.01360	11.7	0.1086	14.6	87.1	104.6	0.80
(13) Titanite 12 gr., Ms, sPr., Gdn. Yw, opaq. incl.	0.3727	9.07	0.35	44.70	32.2	2.1	65.7	0.01422	7.9	0.1254	16.5	91.0	119.9	0.58
(14) Titanite 8 gr., Ms, sPr., Lgt. Yw, opaq. incl.	0.2942	9.48	0.32	44.64	34.2	1.4	64.4	0.01349	10.7	0.0772	19.8	86.4	75.5	0.56
(15) Titanite 10 gr., Ms to Ls, sPr., Gdn. Yw, opaq. incl.	0.3658	10.62	0.40	51.02	32.4	1.7	65.9	0.01397	7.5	0.0988	12.8	89.4	95.6	0.63
TMD 10c-2 (N Tore)														
Titanite														
(16) Titanite ≈10 gr., NA, Ss, Pr. Frag., Lgt. Yw, opaq. incl.	0.2417	9.20	0.27	27.80	43.0	3.1	53.9	0.01441	12.1	0.1452	32.9	92.3	137.7	0.52
(17) Titanite ≈20 gr., NA, Ss, Pr. Frag., Lgt. Yw, opaq. incl.	0.3267	9.69	0.34	36.98	34.2	2.7	63.1	0.01393	7.4	0.1496	25.3	89.1	141.6	0.52
(18) Titanite ≈25 gr., NA, Ss, Pr. Frag., Lgt. Yw, opaq. incl.	0.3960	10.63	0.37	26.74	32.8	2.6	64.6	0.01333	6.6	0.1455	42.0	85.4	137.9	0.64
(19) Titanite ≈15 gr., NA, Ss, Pr. Frag., Lgt. Yw	0.2255	12.45	0.36	37.88	45.2	2.1	52.7	0.01515	15.5	0.0986	30.3	97.0	95.5	0.52
TMD 4-3 (Sponge Bob)														
Titanite														
(20) Titanite 7 gr., NA, Ls to VLs, sPr., Gdn. Yw	0.4524	9.16	0.45	28.58	28.9	1.5	69.6	0.01625	5.9	0.1164	53.4	103.9	111.8	0.58

Table 3 (*continued*)

Sample description[a]	Weight (mg)	Concentration (ppm)		$\frac{^{206}Pb}{^{204}Pb}$	Radiogenic Pb in atomic %[c]			Atomic ratios[c]				Apparent ages Ma[c]		Corr. Coef.
		U	Pb rad.	Meas.[b]	^{206}Pb	^{207}Pb	^{208}Pb	$\frac{^{206}Pb}{^{238}U}$	%err (2σ)	$\frac{^{207}Pb}{^{235}U}$	%err (2σ)	$\frac{^{206}Pb}{^{238}U}$	$\frac{^{207}Pb}{^{235}U}$	
(21) Titanite 7 gr., NA, Ls to VLs, Pr. Frag., Gdn. Yw	0.4502	11.73	0.54	31.97	30.5	1.2	68.3	0.01612	4.4	0.0904	39.6	103.1	87.9	0.49
(22) Titanite 12 gr., NA, Ls, Pr. Frag., Gdn. Yw, opaq. incl.	0.2302	11.90	0.53	30.31	31.1	1.3	67.5	0.01600	7.5	0.0942	38.4	102.3	91.4	0.39
(23) Titanite ≈12 gr., Ms to Ls, Pr. Frag., Gdn. Yw	0.2670	11.86	0.53	30.73	30.6	1.4	68.1	0.01590	7.0	0.0978	45.1	101.7	94.7	0.38
(24) Titanite 5 gr., NA, Ms, Pr. Frag., Gdn. Yw, opaq. incl.	0.2475	11.78	0.54	30.36	30.8	1.9	67.3	0.01639	8.6	0.1356	40.5	104.8	129.1	0.44
(25) Titanite 6 gr., NA, Ms to Ls, LPr., Gdn. Yw	0.2007	12.13	0.55	28.48	30.6	1.1	68.3	0.01608	9.8	0.0796	65.8	102.8	77.8	0.31
Zircon														
(26) Zircon ≈12 gr., Ss, sPr., Nc, opaq. incl.	0.0632	312.74	8.11	440.97	53.7	2.7	43.6	0.01614	0.9	0.1124	1.7	103.2	108.1	0.62
(27) Zircon 5 gr., Ms, sPr., Nc, opaq. incl.	0.0701	237.05	5.80	316.11	56.3	2.7	41.0	0.01597	1.1	0.1060	2.0	102.1	102.3	0.62
(28) Zircon ≈14 gr., Ss, sPr., Nc, opaq/ap. incl.	0.0942	289.67	8.23	393.10	53.0	2.8	44.3	0.01745	3.7	0.1250	4.2	111.5	119.6	0.90
TMD 4-8 (Sponge Bob)														
Titanite														
(29) Titanite ≈10 gr., NA, мs, Pr. Frag., Gdn. Yw, opaq. incl.	0.1822	11.60	0.49	22.67	33.3	1.7	65.0	0.01634	5.7	0.1144	74.2	104.5	110.0	0.74
(30) Titanite 6 gr., NA, Ms to Ls, Pr. Frag., Gdn. Yw	0.3526	12.48	0.61	22.73	27.5	1.4	71.1	0.01560	3.8	0.1065	61.6	99.8	102.8	0.87
(31) Titanite 4 gr., NA, Ls to VLs, Pr. Frag., Gdn. Yw	0.3684	12.95	0.66	22.21	27.0	0.1	71.9	0.01585	3.3	0.0895	59.5	101.4	87.0	0.75
(32) Titanite 8 gr., Ms to Ls, Pr. Frag., Gdn. Yw	0.3764	12.86	0.68	24.62	26.8	1.4	71.8	0.01634	3.5	0.1190	40.5	104.5	114.1	0.65
(33) Titanite 6 gr., Ls, Pr. Frag., Gdn. Yw	0.3674	12.27	0.64	28.62	27.1	1.0	71.9	0.01622	2.8	0.0834	30.6	103.7	81.3	0.47
(34) Titanite 8 gr., Ms to Ls, Pr. Frag., Gdn. Yw	0.3182	12.02	0.65	26.09	27.3	1.3	71.4	0.01701	2.4	0.1109	16.7	108.7	106.8	0.45
TMD 14-9 (Ashton)														
Titanite														
(35) Titanite 1 gr., VLs, sPr., Gdn. Yw	0.5448	9.99	0.47	34.32	26.8	1.2	72.0	0.01459	4.4	0.0876	43.2	93.4	85.3	0.53
(36) Titanite 11 gr., Ms, Pr. Frag., Gdn. Yw	0.1908	8.33	0.30	29.66	35.0	2.2	62.8	0.01454	11.9	0.1286	29.3	93.0	122.8	0.51
(37) Titanite 3 gr., NA, Ls, sPr., Gdn. Yw, opaq. incl.	0.1898	8.44	0.33	27.98	32.3	2.4	65.2	0.01454	9.7	0.1502	9.7	93.1	142.1	0.51
(38) Titanite 10 gr., Ms, Pr. Frag., Gdn. Yw, opaq. incl.	0.1165	8.96	0.28	27.20	40.2	2.2	57.6	0.01466	15.6	0.1120	15.6	93.8	107.8	0.44
(39) Titanite ≈20 gr., Ss, Pr. Frag., Gdn. Yw, opaq. incl.	0.3374	8.79	0.38	30.64	29.3	1.4	69.3	0.01481	5.9	0.0974	46.9	94.8	94.4	0.51

(40) Titanite 1 gr., VLs, sPr., Gdn. Yw	0.3802	8.77	0.35	33.15	32.0	1.7	66.3	0.01479	6.0	0.1088	37.9	94.6	104.8	0.48
(41) Titanite 4 gr., NA, Ls to VLs, sPr., Gdn. Yw	0.3082	8.77	0.36	35.26	33.4	2.1	64.5	0.01593	14.0	0.1384	44.3	101.9	131.6	0.48
(42) Titanite 1 gr., VLs, sPr., Gdn. Yw	0.2570	8.47	0.34	29.90	32.5	1.8	65.7	0.01497	7.8	0.1142	44.4	95.8	109.8	0.49
Zircon														
(43) Zircon 4 gr., Ms, sPr., Nc	0.2142	56.06	1.05	323.70	69.2	3.3	27.5	0.01508	1.3	0.1000	2.2	96.5	96.8	0.66
(44) Zircon 6 gr., Ss, sPr. Nc, opaq/ap. incl.	0.0886	53.39	1.09	117.82	64.2	3.1	32.8	0.01525	4.0	0.1005	9.1	97.6	97.3	0.53
(45) Zircon 4 gr., Ms, sPr., Nc	0.0991	76.12	1.57	152.32	64.2	3.4	32.4	0.01531	3.1	0.1109	4.6	97.9	106.8	0.72
TMD 15-5 (Gago Coutinho)														
Titanite														
(46) Titanite 8 gr., Ms, Pr. Frag., Gdn. to Dk Yw	0.1296	14.10	0.46	27.99	37.0	3.0	60.1	0.01402	8.7	0.1545	34.7	89.7	145.9	0.54
(47) Titanite 12 gr., Ms, Pr. Frag., Lgt. Yw, opaq. incl.	0.1350	13.16	4.7	0.37	44.9	2.7	52.4	0.01480	11.0	0.1221	17.3	94.7	117.0	0.65
(48) Titanite 15 gr., Ms, Pr. Frag.,Lgt. to Dk Yw, opaq. incl.	0.1975	12.11	0.41	35.35	36.2	2.0	61.8	0.01425	9.4	0.1066	29.2	91.2	102.8	0.44
(49) Titanite 15 gr., Ms, Pr. Frag., Lgt. to Dk Yw, opaq. incl.	0.1854	14.47	0.50	36.17	36.8	2.7	60.5	0.01473	7.9	0.1483	18.4	94.2	140.4	0.56
(50) Titanite 20 gr., Ss, Pr. Frag., Lgt. Yw, opaq. incl.	0.2430	14.74	0.56	40.44	33.0	1.6	65.4	0.01440	9.3	0.0941	18.4	92.2	91.3	0.55
TMD 16-1 (Jo Sister)														
Titanite														
(51) Titanite 10 gr., Ss, Pr. Frag., Lgt Gdn. Yw, opaq.incl.	0.2053	9.95	0.31	35.56	38.2	2.1	59.7	0.01394	12.0	0.1058	33.6	89.2	102.1	0.45
(52) Titanite 15 gr., NA, Ss, Pr. Frag., Lgt Gdn. Yw, opaq. incl.	0.2377	10.06	0.32	36.79	37.2	2.3	60.5	0.01359	10.4	0.1158	19.8	87.0	111.2	0.58
(53) Titanite 25 gr., Ss, Pr. Frag.,Lgt Gdn. Yw, opaq.incl.	0.2567	10.07	0.34	30.64	35.5	2.1	62.5	0.01366	8.7	0.1106	22.8	87.5	106.5	0.50
(54) Titanite 9 gr., Ms, sPr., Lgt Gdn. Yw, opaq. incl.	0.2485	10.80	0.32	38.09	39.5	2.0	58.5	0.01336	9.6	0.0954	23.0	85.6	92.5	0.50
(55) Titanite 14 gr., Ms, sPr., Lgt Gdn. Yw, opaq. incl.	0.3621	10.86	0.35	39.58	36.0	1.8	62.2	0.01336	6.3	0.0918	23.8	85.6	89.2	0.44

Table 3 (*continued*)

Sample description[a]	Weight (mg)	Concentration (ppm)		$\frac{^{206}Pb}{^{204}Pb}$	Radiogenic Pb in atomic %[c]			Atomic ratios[c]				Apparent ages Ma[c]		Corr. Coef.
		U	Pb rad.	Meas.[b]	^{206}Pb	^{207}Pb	^{208}Pb	$\frac{^{206}Pb}{^{238}U}$	%err (2σ)	$\frac{^{207}Pb}{^{235}U}$	%err (2σ)	$\frac{^{206}Pb}{^{238}U}$	$\frac{^{207}Pb}{^{235}U}$	
TMD 16-2 (Jo Sister)														
Titanite														
(56) Titanite ≈10 gr., Ss to Ms, Pr. Frag., Gdn. Yw, opaq. incl.	0.2462	10.79	0.33	31.07	39.7	2.2	58.0	0.01402	6.9	0.1090	34.6	89.8	105.1	0.47
(57) Titanite ≈12 gr., Ss, Pr. Frag., Gdn. Yw, opaq. incl.	0.2716	10.80	0.38	28.75	40.1	1.9	63.0	0.01435	9.4	0.1073	49.8	91.8	103.5	0.44
(58) Titanite 18 gr., NA, Ss, Pr. Frag., Lgt Gdn. Yw, opaq. incl.	0.3664	10.92	0.36	29.99	37.1	2.6	60.3	0.01423	5.2	0.1396	39.9	91.1	132.7	0.67
(59) Titanite ≈20 gr., NA, Ss, Pr. Frag., Gdn. Yw, opaq. incl.	0.3642	9.99	0.34	30.94	35.1	1.6	63.3	0.01372	5.2	0.0877	46.4	87.8	85.3	0.53
(60) Titanite 6 gr., Ms to Ls, sPr., Gdn. Yw, opaq. incl.	0.2430	10.21	0.33	40.63	41.5	2.0	56.6	0.01548	11.8	0.1008	33.6	99.0	97.5	0.45
(61) Titanite 8 gr., Ms, sPr., Gdn. Yw, opaq. incl.	0.1110	10.82	0.25	29.38	51.6	3.5	44.9	0.01354	18.3	0.1265	30.4	86.7	120.9	0.61
(62) Titanite 10 gr., Ss, Pr. Frag., Gdn. Yw, opaq. incl.	0.2134	10.41	0.32	29.89	37.5	2.1	60.4	0.01315	11.9	0.1017	39.5	84.2	98.3	0.45
(63) Titanite 10 gr., Ss to Ms, Pr. Frag., Gdn. Yw, opaq. incl.	0.2066	11.98	0.35	34.12	40.8	2.8	56.4	0.01365	12.9	0.1291	25.0	87.4	123.3	0.57
(64) Titanite ≈20 gr., NA, Ms, Pr. Frag., Lgt Yw, opaq. incl.	0.3099	10.47	0.32	36.27	37.8	2.3	59.9	0.01355	7.3	0.1144	33.8	86.8	110.0	0.48

[a] Analyses were performed on transparent, euhedral titanites and zircons. NA, non-abraded (all other minerals mechanically abraded, following the technique described by Krogh (1982)). Gr., grains; Ss, small size (100–150 μm); Ms, middle size (150–200 μm); Ls, large size (200–250 μm); VLs, very large size (>250 μm); Pr. Frag., prismatic fragment; sPr., short prismatic (length/width = 2 to 4); Yw, yellow; Dk., dark; Lgt., light, Gd., golden; Pl., pale; Nc, no color; opaq. incl., opaque inclusions, opaq/ap. incl., opaque and/or apatite inclusions. Mass discrimination is 0.10 ± 0.05%/amu for both Pb and U. Decay constants for ^{238}U and ^{235}U are thoses determined by Jaffey et al. (1971) and recommended by Steiger and Jäger (1977): $^{238}U = 1.55125 \times 10^{-10}$ y^{-1} ± 8.33 × 10^{-14} (0.054%), $^{235}U = 9.84850 \times 10^{-10}$ y^{-1} ± 6.71 × 10^{-13} (0.068%). Total Pb blanks are from 60 to 100 pg for titanite and from 20 to 34 pg for zircon. Total procedural U blanks are less than 1 pg in both procedures (see analytical procedures for details). [b] Ratios corrected for mass-discrimination and isotopic tracer. [c] Ratios corrected for mass-discrimination, isotopic tracer contribution, blank, and initial common Pb determined in leached K-fsp and Plag. from the same rock sample (Table 5).

Table 4
Isochron U–Pb data for the titanite fractions from the rock samples from the different seamounts

Samples	Concentration Pb comm. (ppm)	$^{206}Pb/^{204}Pb^{(a)}$ (α)	Error in % (2σ-STERR)	238/204[a] (μ)	Error in % (2σ-STERR)
TMD 3b-2 (NW Tore)					
(1) Titanite	0.357	49.29	1.03	2467	1.11
(2) Titanite	0.257	64.66	0.65	3418	1.50
(3) Titanite	0.286	61.59	0.42	3360	4.74
(4) Titanite	0.231	74.94	0.87	4344	1.50
(5) Titanite	0.075	181.85	0.64	12761	1.82
(6) Plag.		19.14	0.07	—	—
TMD 10c-1 (N Tore)					
(7) Titanite	0.433	38.64	0.81	1443	0.96
(8) Titanite	0.099	109.01	1.47	6411	1.57
(9) Titanite	0.076	134.09	0.83	8425	0.50
(10) Titanite	0.158	72.72	1.14	3743	0.91
(11) Titanite	0.117	90.84	0.78	5287	0.54
(12) Titanite	0.134	91.67	0.59	5168	0.71
(13) Plag.		19.50	0.11	—	—
TMD 10c-2 (N Tore)					
(14) Titanite	0.543	35.22	0.57	1101	0.87
(15) Titanite	0.304	48.21	1.63	2072	1.47
(16) Titanite	0.938	29.17	0.35	737.1	0.62
(17) Plag.		19.34	0.08	—	—
TMD 4-3 (Sponge Bob)					
(18) Titanite	0.829	31.21	1.02	722.3	1.32
(19) Titanite	0.775	35.43	0.43	989.8	0.36
(20) Titanite	0.745	36.19	0.44	1045	0.50
(21) Titanite	0.736	36.23	0.74	1053	0.51
(22) Titanite	0.718	37.05	1.19	1072	1.32
(23) Titanite	0.842	34.63	0.71	942.6	1.33
(24) K-fsp		19.47	0.13	—	—
TMD 4-8 (Sponge Bob)					
(24) Titanite	3.43	23.27	0.66	223.3	0.98
(25) Titanite	3.83	22.98	0.52	215.3	1.13
(26) Titanite	4.32	22.75	0.32	197.7	1.13
(27) Titanite	2.49	25.19	0.55	340.6	0.88
(28) Titanite	1.26	30.00	0.54	640.2	0.51
(29) Titanite	1.85	26.93	0.17	429.9	0.50
(30) K-fsp		19.62	0.21	—	—
TMD 14-9 (Ashton)					
(31) Titanite	0.503	38.20	0.74	1291	0.48
(32) Titanite	0.394	39.35	0.42	1374	0.50
(33) Titanite	0.563	33.54	0.52	974.9	0.41
(34) Titanite	0.496	36.56	0.96	1172	0.61
(35) Titanite	0.556	34.59	0.54	1027	0.72
(36) Titanite	0.437	38.66	0.93	1305	1.15
(37) Titanite	0.516	35.32	0.94	1066	1.09
(38) K-fsp		19.36	0.04	—	—
TMD 15-5 (Gago Coutinho)					
(39) Titanite	0.977	32.63	0.65	941.3	0.38
(40) Titanite	0.309	60.50	0.24	2775	0.36
(41) Titanite	0.368	50.01	0.97	2145	1.17
(42) Titanite	0.482	48.27	0.55	1958	0.41
(43) Titanite	0.309	64.24	0.34	3110	0.91
(44) K-fsp		19.44	0.03	—	—
TMD 16-1 (Jo Sister)					
(45) Titanite	0.241	56.61	0.60	2730	0.50
(46) Titanite	0.316	47.97	0.51	2084	0.45
(47) Titanite	0.242	58.44	0.81	2914	0.97
(48) Titanite	0.288	52.45	0.78	2465	0.52
(49) K-fsp		19.50	0.05	—	—
TMD 16-2 (Jo Sister)					
(49) Titanite 9	0.572	36.81	0.42	1234	0.55

Table 4 (*continued*)

Samples	Concentration Pb comm. (ppm)	$^{206}Pb/^{204}Pb^{(a)}$ (α)	Error in % (2σ-STERR)	238/204$^{(a)}$ (μ)	Error in % (2σ-STERR)
(50) Titanite 10	0.661	34.85	0.88	1069	1.04
(51) Titanite 11	0.770	32.71	0.98	928.7	1.42
(52) Titanite 12	0.597	34.53	0.30	1095	0.33
(53) Titanite 17	0.349	46.96	0.82	2028	4.06
(54) Titanite 19	0.449	39.45	0.89	1517	1.29
(55) Titanite 20	0.311	53.93	0.99	2523	1.03
(56) Titanite 22	0.332	47.44	1.74	2062	0.95
(57) K-fsp		19.50	0.06	—	—

For each rock, initial Pb ratios were measured in plagioclases and K-fsp from the same rock (Table 5). [a] Ratio corrected for mass discrimination, isotopic tracer contribution, and Pb blank.

Table 5
Pb analytical results for feldspars of the different dated seamounts

Samples	Mineral	$(^{206}Pb/^{204}Pb)_i$	$(^{207}Pb/^{204}Pb)_i$	$(^{208}Pb/^{204}Pb)_i$	Source		
					μ	ω	κ
Tore seamount							
TMD3b-2	Plag	19.139 ± 0.013	15.544 ± 0.012	38.750 ± 0.030	9.68	37.23	3.85
TMD10c-1	Plag	19.496 ± 0.021	15.611 ± 0.021	39.281 ± 0.050	10.04	39.42	3.93
TMD10c-2	Plag	19.343 ± 0.016	15.642 ± 0.014	39.310 ± 0.025	9.89	39.54	4.00
Sponge Bob seamount							
TMD4-3	K-fsp	19.471 ± 0.025	15.714 ± 0.020	39.496 ± 0.049	10.04	40.41	4.03
TMD4-8	K-fsp	19.620 ± 0.042	15.828 ± 0.040	39.936 ± 0.109	10.19	42.19	4.14
Ashton seamount							
TMD14-9	K-fsp	19.363 ± 0.007	15.636 ± 0.006	39.179 ± 0.015	9.92	39.08	3.94
Gago Coutinho seamount							
TMD15-5	K-fsp	19.440 ± 0.006	15.661 ± 0.010	39.377 ± 0.028	9.99	39.84	3.99
Jo Sister seamount							
TMD16-1	K-fsp (microlite)	19.497 ± 0.009	15.652 ± 0.007	39.517 ± 0.016	10.04	40.36	4.02
TMD16-2	K-fsp (microlite)	19.496 ± 0.012	15.669 ± 0.009	39.552 ± 0.026	10.04	40.52	4.04

Plagioclases were spiked with the $^{233}U-^{235}U-^{205}Pb$ tracers to U/Pb. No significant amount of U was detected. Isotopic ratios were determinated with a VG sector instrument using a Faraday cup and a Thomson 206 instrument using a Faraday cup and an electron multiplier system. For both instruments, the Faraday cups were used. All μ ($^{238}U/^{204}Pb$), ω ($^{232}Th/^{204}Pb$) and κ ($^{232}Th/^{238}U$) values were calculated for the U–Pb Concordia age of the same rock (Table 3) using a single-stage evolution model of the Earth mantle (Holmes, 1946). For these calculations, constants used are recommended by IUGS (Steiger and Jäger, 1977); an age of 4.56 Ga was used for the Earth (Allègre et al., 1995) and initial Pb composition measured in Canyon Diablo iron meteorite (Tatsumoto et al., 1973).

mean $^{206}Pb/^{238}U$ age of 89.3 ± 2.3 Ma (Fig. 8e). The titanite–K-fsp. $^{238}U/^{204}Pb-^{206}Pb/^{204}Pb$ isochron age is 88.3 ± 1.3 Ma (Fig. 8f).

7.3. Pb–Sr–Hf isotope results

Pb, Sr, and Hf isotope data are summarized in the Tables 5–7, and plotted in the Figs. 9–12 together with data fields for Atlantic MORB, the latest Miocene to Quaternary São Miguel Island, the 14 Ma to recent Madeira Archipelago, and in particular, Ormonde and Monchique Cretaceous alkaline magmatism (Fig. 1). Where appropriate, data for worldwide OIB were also included as well as data from the Ampere, Seine, and Unicorn seamounts (Fig. 1). Initial Hf signatures are plotted *vs.* time in Fig. 11, together with evolution model curves for depleted MORB mantle (DM) and chondrite uniform mantle reservoir (CHUR).

8. Discussion

8.1. Geochronology

Since the U–Pb chronometer in zircon and titanite behave as closed systems at temperatures in excess to 700 °C (e.g., Krogh, 1973; Zhang and Schärer, 1996), all ages given in both the Concordia and isochron diagrams can be interpreted to date the crystallization of these minerals either in the magma chamber from where magmas were extracted or *in situ*, within the solidifying lava. Time intervals between chamber or lava crystallization can be considered to be short, compared to analytical uncertainties on the ages. Investigations of magma transfer kinetics show that these processes are very rapid occurring on the order of 100–200 ky (e.g. Condomines et al., 1982). Zircon data from two trachytes (Figs. 6a and 7a) substantiate the presence of very small amounts of older inherited zircon

Table 6
Rb–Sr analytical results for feldspars from the different seamount samples

Samples	Weight (mg)	Concentrations		$^{87}Rb/^{86}Sr \pm 2\%$	Concordia age (Ma)	$^{87}Sr/^{86}Sr$ measured	$(^{87}Sr/^{86}Sr)_i$
		Sr (ppm)	Rb (ppm)				
Tore seamount							
TMD3b-2	9.95	459	2.39	0.0152	80.5	0.70308 ± 1	0.70306
TMD10c-1	9.34	630	0.51	0.0024	88.3	0.70341 ± 1	0.70340
TMD10c-2	8.03	705	0.53	0.0022	88.2	0.70294 ± 2	0.70294
Sponge Bob seamount							
TMD4-3	8.95	14.3	49.7	10.2	102.8	0.70869 ± 2	0.69396*
Duplicate	8.31	11.8	39.0	9.70	102.8	0.70928 ± 2	0.69528*
TMD4-8	8.46	72.7	23.6	0.951	104.4	0.70371 ± 3	0.70231
Ashton seamount							
TMD14-9	9.30	257	8.22	0.0935	96.3	0.70321 ± 1	0.70309
Gago Coutinho seamount							
TMD15-5	9.00	372	3.73	0.0294	92.3	0.70309 ± 1	0.70305
Jo Sister seamount							
TMD16-1	8.13	113	25.5	0.6596	86.5	0.70360 ± 4	0.70280
TMD16-2	9.20	69.4	29.9	1.26	89.3	0.70401 ± 3	0.70243

Measured $^{87}Sr/^{86}Sr$ ratios were normalized to $^{86}Sr/^{88}Sr = 0.1194$. Analytical uncertainties are $\pm 2\%$ for $^{87}Rb/^{86}Sr$. Uncertainties for measured $^{87}Sr/^{86}Sr$ are given in table relative to the last digits. The ^{87}Rb decay constant used to calculate $^{87}Sr/^{86}Sr_{(i)}$ is $1.42 \times 10^{-11}y^{-1}$(Steiger and Jäger, 1977). Rb and Sr concentration were performed on a Thomson 206 mass-spectrometer using electron multiplier and a single Faraday cup. Isotopic compositions of Sr were performed on a VG sector mass-spectrometer using a single Faraday cup. *, overcorrection from high $^{87}Rb/^{86}Sr$.

Table 7
Hf isotope analytical results for the dated zircons of the different seamount samples

Samples	$^{176}Hf/^{177}Hf$ measured	Concordia age (Ma)	εHf_0 (present day)	εHf_i
Tore seamount				
TMD 3b-2 Z1	0.282983 ± 8	80.5	7.5	9.3 ± 0.3
TMD 3b-2 Z2	0.283084 ± 7	80.5	11.0	12.9 ± 0.2
TMD 3b-2 Z3	0.282996 ± 11	80.5	7.9	9.7 ± 0.4
Sponge Bob seamount				
TMD 4-3 Z1	0.282966 ± 8	102.8	6.9	9.2 ± 0.3
TMD 4-3 Z2	0.282901 ± 8	102.8	4.6	6.9 ± 0.3
Ashton seamount				
TMD 14-9 Z1	0.282965 ± 5	96.3	6.8	9.0 ± 0.2
TMD 14-9 Z2	0.282953 ± 8	96.3	6.4	8.6 ± 0.3
TMD 14-9 Z3	0.282942 ± 7	96.3	6.0	8.2 ± 0.2

Measured $^{176}Hf/^{177}Hf$ are corrected for mass-discrimination using $^{179}Hf/^{177}Hf = 0.7325$ (Patchett and Tatsumoto, 1980). JMC- 475 Hf standard: $^{176}Hf/^{177}Hf = 0.282163 \pm 9$ (Blichert-Toft et al., 1997). To calculate epsilon values (εHf_0 and εHf_i) the following constants were used: age of the Earth = 4.56 Ga; $(^{176}Lu/^{177}Hf)^0_{CHUR} = 0.0332 \pm 2$; $(^{176}Hf/^{177}Hf)CHUR$ today = 0.282772 ± 29; $(^{176}Hf/^{177}Hf)CHUR$ at 4.56 Ga = 0.279718 ± 29 (Blichert-Toft and Albarède, 1997); $\varepsilon Hf^T_{sample} = [(^{176}Hf/^{177}Hf)^T_{sample}/(^{176}Hf/^{177}Hf)^T_{CHUR} - 1] \times 10^4$, with $(^{176}Hf/^{177}Hf)^T_{CHUR} = (^{176}Hf/^{177}Hf)^0_{CHUR} - (^{176}Lu/^{177}Hf)^0_{CHUR} \times (e^{\lambda T} - 1)$ (Patchett et al., 1981); $\lambda_{Lu} = 1.93 \times 10^{-2}$ Ga^{-1} (Sguigna et al., 1982).

incorporated into the host magma. Such inheritance in mantle-derived rocks has also been observed for dikes intruding the ultramafic–mafic complex of the Ligurian Alps, where relic zircons appears to have been extracted from the subcontinental lithospheric mantle, tapped by asthenospheric magmas (Borsi et al., 1996). Alkali lavas (77 Ma) on top of the Ormonde seamount also shows zircon inheritance (Schärer et al., 2000).

The available U–Pb dates show that seamount genesis along the continent–ocean transition of the Iberian margin (Fig. 1) occurred over a period of at least 23.9 ± 1.2 m.y.

bracketed by the oldest seamount dated at 104.4 ± 1.4 Ma (107.2 ± 3.4 Ma for isochron), and 80.5 ± 0.9 Ma (82.0 ± 2.4 Ma for isochron) for the youngest. This implies that alkaline magmatism occurred roughly 21 m.y. after formation of the first Atlantic oceanic crust around 125–130 Ma (Gradstein et al., 2004). In consequence, construction of the seamounts cannot be attributed to Atlantic spreading as proposed earlier; they should be considered to reflect an exclusively intra-plate phenomena. An important time gap of about 70 m.y. exists between 104–81 Ma seamount emplacement along the northern segment of
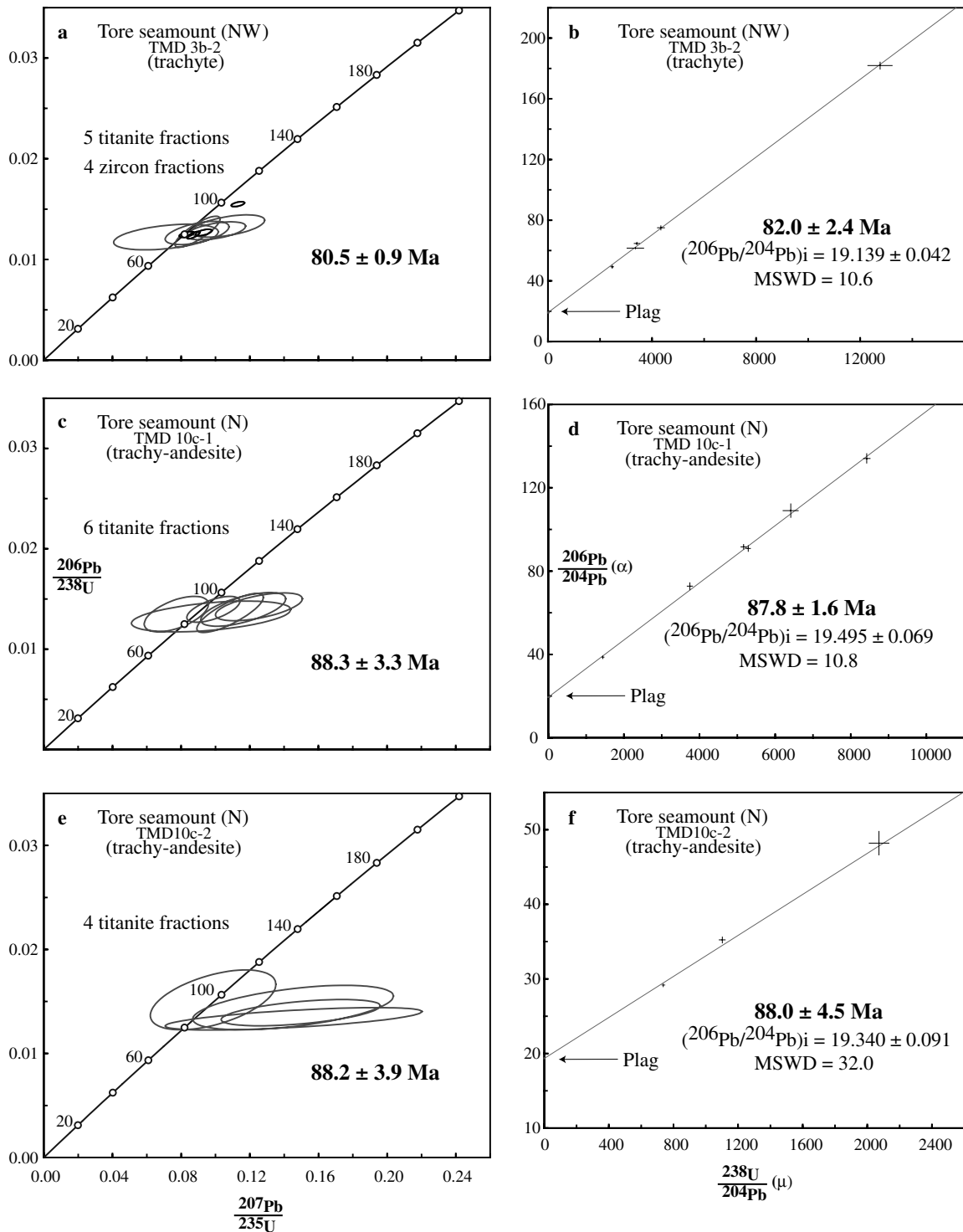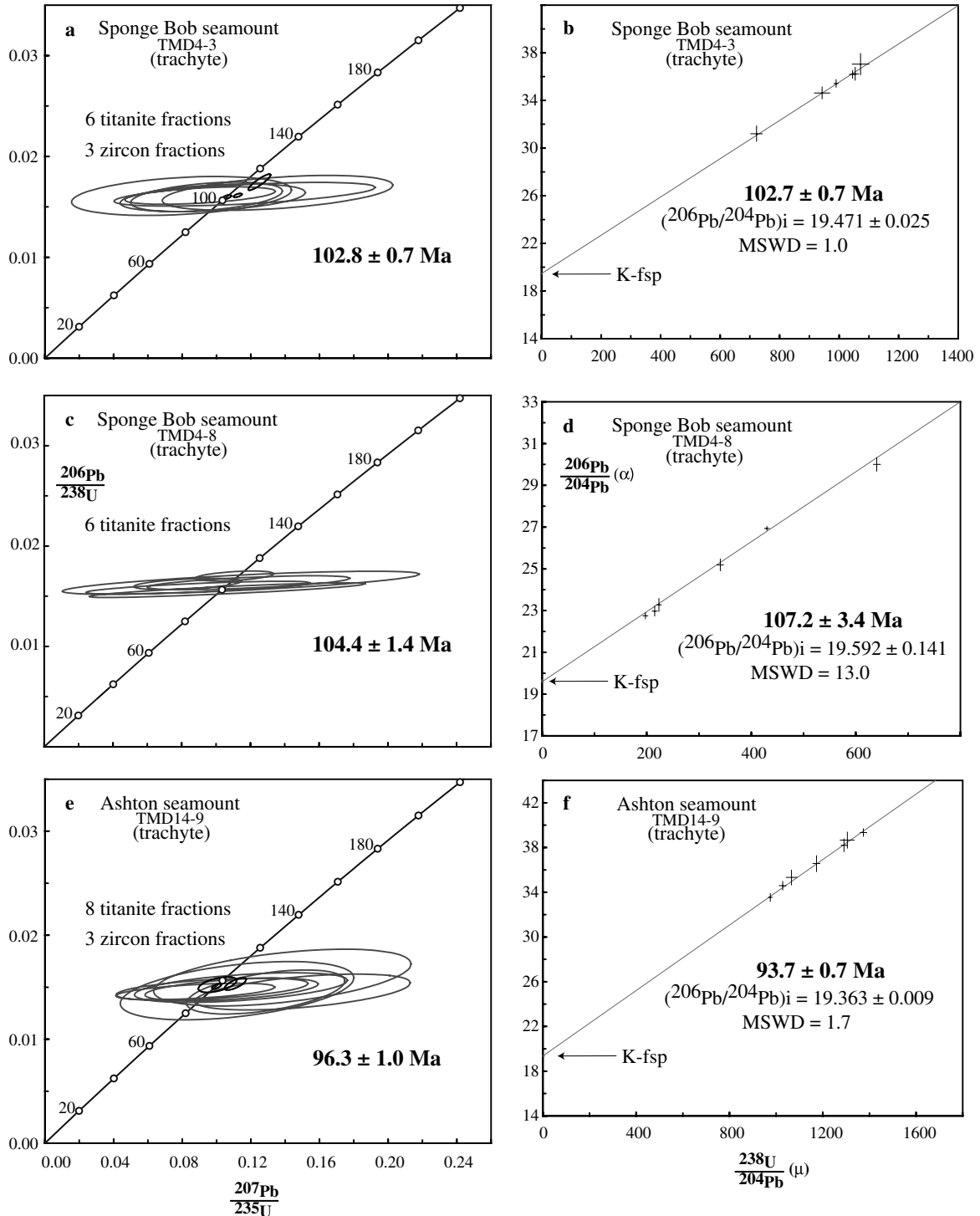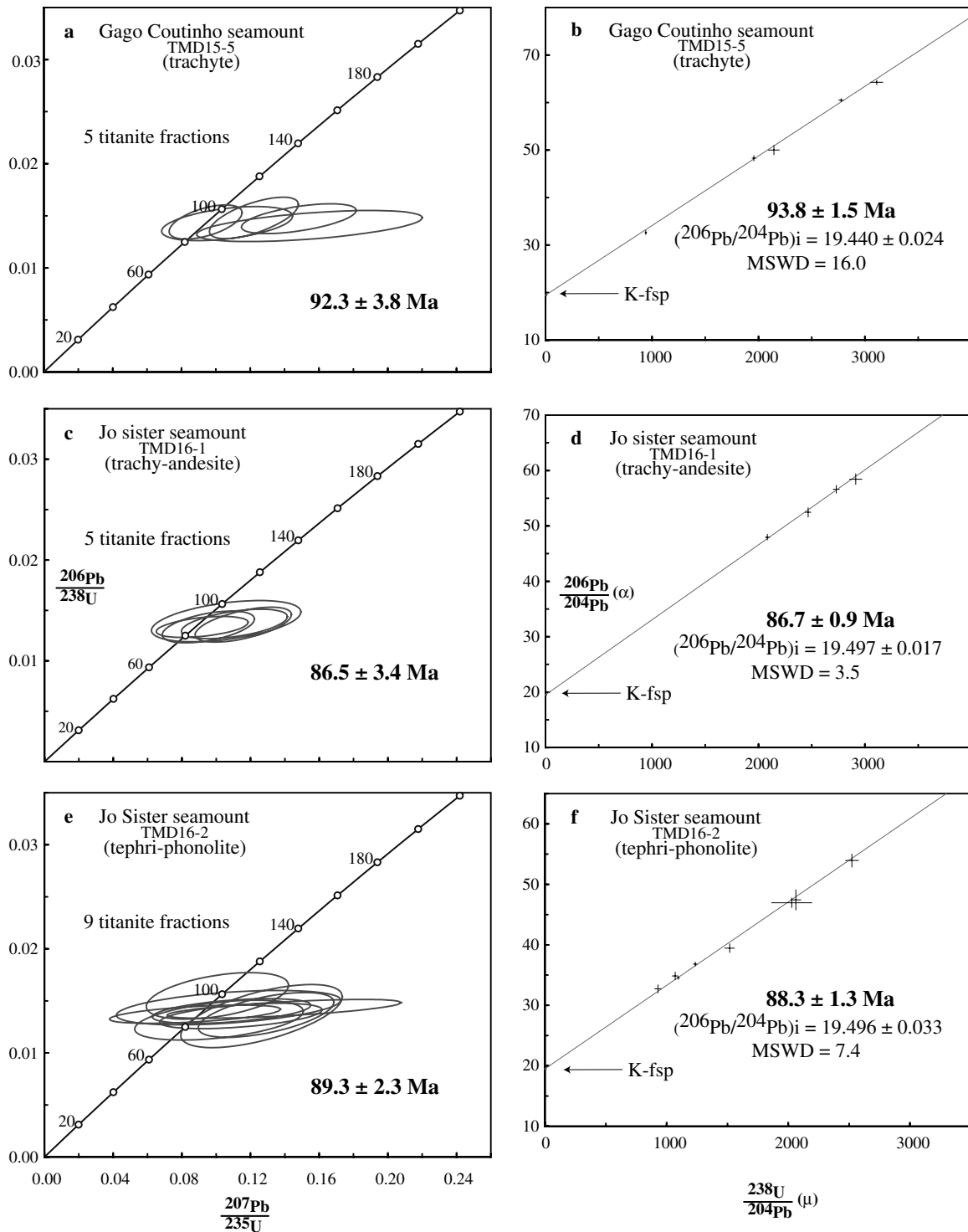
Fig. 6. Concordia and isochron plots of U–Pb dating results of titanite and zircon. Ellipses correspond to 2σ-STERR. Symbols in the isochron plots are two times larger than relative errors. Zircon fractions represented by thick ellipses.

the Tore-Madeira Rise, and the much younger, 14 Ma to recent formation of the Madeira Archipelago. The Cretaceous volcanic phases dated in this study could potentially be followed by Miocene to recent volcanism, as suggested by earlier K–Ar dating of Wendt et al. (1976) from the Josephine seamount. New $^{40}Ar/^{39}Ar$ data from this seamount and a further two seamounts south of Josephine give ages between 0.5 and 16 Ma (Geldmacher et al., in press). These date corroborate the genesis of the Tore Madeira rise to be significantly more complex than previously thought. For instance, very contrasting ages of 86–89 Ma vs. 4 Ma indicate two very distinct phases of Jo Sister magmatic activity in Late Cretaceous and Pliocene times. Considering the sensitivity of whole-rock matrix to

Fig. 7. Concordia and isochron plots of U–Pb dating results of titanite and zircon. Ellipses correspond to 2σ-STERR. Symbols in the isochron plots are two times larger than relative errors. Zircon fractions represented by thick ellipses.

seawater interactions, K–Ar and $^{40}Ar/^{39}Ar$ whole-rock ages from these seamounts require confirmation.

8.2. Petrogenesis of samples

All samples studied here are evolved alkaline lavas whose compositions range from trachy-andesite to tra-chyte, which cannot be derived by simple partial melting of peridotites. To explain their origin the following options have to be considered: (1) differentiation by crystal frac-tionation from an originally alkali-basaltic liquid, (2) small degrees of melting of non-peridotite sources, and (3) mix-ing of alkali-basaltic liquids with highly differentiated mag-mas having SiO_2 above 65 wt%. Note that the most evolved

Fig. 8. Concordia and isochron plots of U–Pb analytical results of titanite and zircon. Ellipses correspond to 2σ-STERR. Symbols in the isochron plots are two times larger than relative errors.

rock analyzed here is a trachyte with 63.4 wt% SiO₂ (Table 2). To evaluate these possibilities it is useful to recall the following: (a) about half of the dredged samples are trachy-andesites and trachytes, whereas the remaining rocks are basanites and alkali-basalts; (b) the lavas studied here have experienced different degrees of crystal fractionation prior to extrusion, as indicated by anomalies in Ti, P, Sr

and Ba (Fig. 4). These anomalies can be ascribed to fractional crystallization of Fe–Ti oxides, apatite and feldspar. Plagioclase fractionation is corroborated by strong depletion in Sr and modestly negative Eu anomalies in some samples (Figs. 4 and 5). Some of the lavas are plagioclase cumulative as indicated by their slightly positive Eu anomalies.
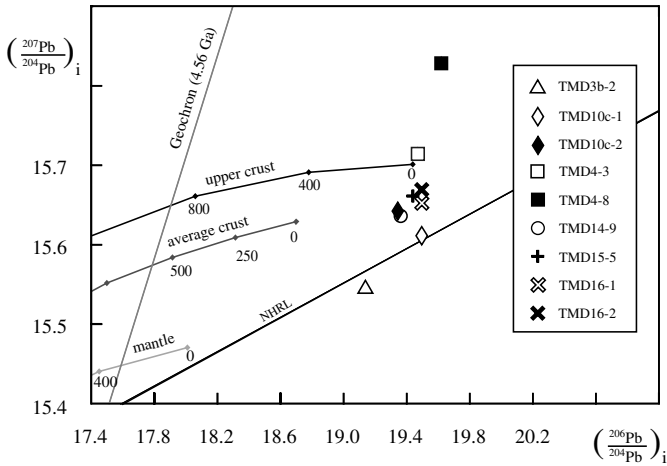
Fig. 9. $^{206}Pb/^{204}Pb$ vs. $^{207}Pb/^{204}Pb$ diagram of initial Pb isotopic composition measured in feldspars from the dated samples. Accuracy (2σ) of individual data are within the size of the symbols. The model curves for a single-stage evolution of the Earth (Geochron; Holmes, 1946), a multi-stage evolution of the Earth mantle, version II (Zartman and Doe, 1981), the evolution of the upper continental crust, version II (Zartman and Doe, 1981), and the model for average continental crust (Stacey and Kramers, 1975) are given for reference. The samples studied are represented with the same legend as in Fig. 3.

Storage for a considerable period of time of liquids in magma chambers may lead to wallrock assimilation, in particular the Iberian subcontinental mantle. Alternatively, "en route" contamination during magma ascent through this lithosphere could also occur. Arguments in favor of this are (1) the small components of inherited Pb present in a few zircons (Figs. 6a and 7a), (2) differences in initial Hf among zircons from a single rock (Fig. 11), and (3) relatively radiogenic common Pb, in particular ^{207}Pb which does not match any MORB or OIB mantle reservoir. Cases of high initial $^{207}Pb/^{204}Pb$ of subcontinental mantle are also reported for lherzolithe xenoliths of recent volcanic rocks from Tanzania, E-Africa (Cohen et al., 1984).

8.3. Isotope characteristics

Initial Pb isotopic compositions (Fig. 9) are significantly more radiogenic than a single stage model (Geochron) and they roughly plot at the end or beyond the model evolution curve for upper continental crust (Zartman and Doe, 1981). Their variation is relatively limited in $^{206}Pb/^{204}Pb$ ranging from 19.139 to 19.620, whereas variations in $^{207}Pb/^{204}Pb$ are significantly larger lying between 15.544 and 15.828. Plotted in an $^{206}Pb/^{204}Pb$–$^{207}Pb/^{204}Pb$ diagram (Fig. 10a) the data range from the Atlantic field for NW-Tore to significantly more radiogenic values. The same data trends are present in the $^{206}Pb/^{204}Pb$–$^{208}Pb/^{204}Pb$ diagram (Fig. 10b) lying sub-parallel to data field from São Miguel Island of the Azores Archipelago (Widom et al., 1997; Moreira et al., 1999). A heterogeneous plume, containing in addition an old subcontinental lithospheric mantle was proposed for the origin of the São Miguel Island (Widom et al., 1997; Moreira et al., 1999). Lead of 3 sea-
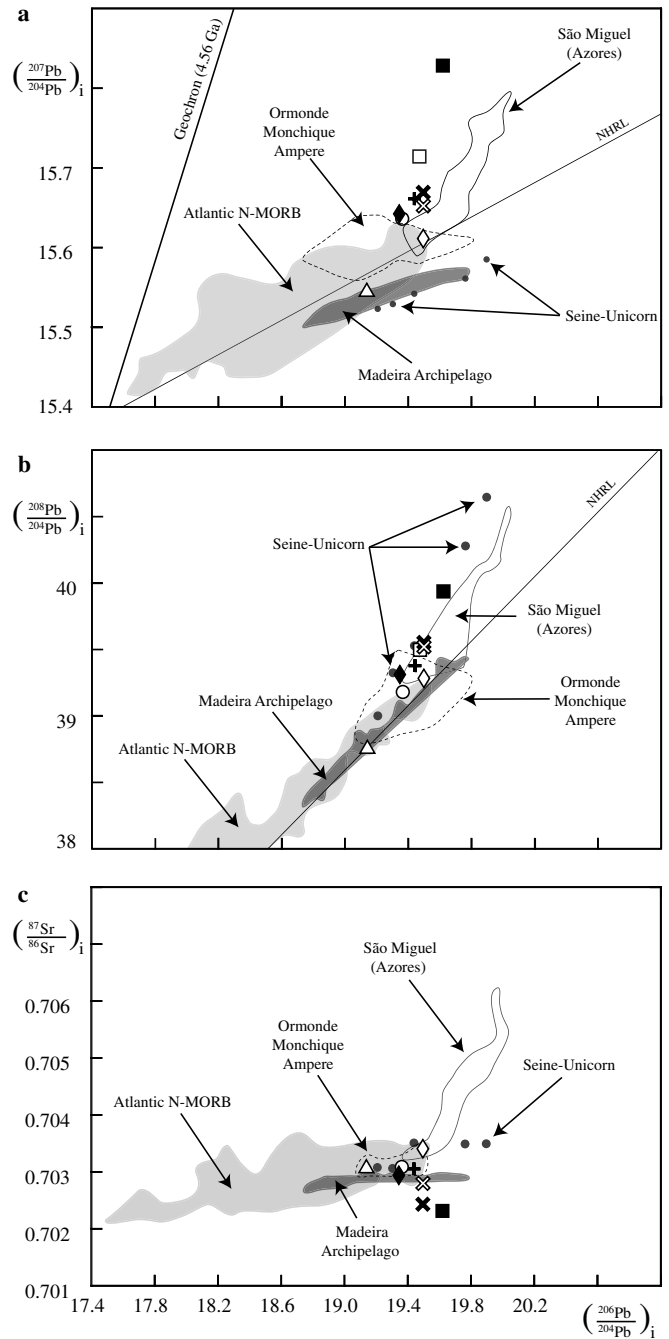

Fig. 10. Initial Pb–Pb and Pb–Sr isotopes diagrams. Data are shown relative to the present day data fields of Atlantic N-MORB, the Madeira Archipelago and São Miguel Island of the Azores Archipelago (PetDB and GEOROC databases). Also shown are data for the Monchique and Ormonde alkaline rocks (Bernard-Griffiths et al., 1997), as well for the seamounts at Ampere, Coral Patch, Seine, and Unicorn (Geldmacher and Hoernle, 2000; Geldmacher et al., 2005).

mounts (NW and N-Tore and Ashton) lies in the field of Atlantic MORB. Most initial $^{87}Sr/^{86}Sr$ values range from 0.70232 to 0.70340. A sample yields unreasonable low ratios below 0.70 (TMD4-3, Table 6). Since our single feldspars grains show very weak alteration features, it may be that apparent opening of the Rb–Sr system could be related to seawater alteration. In our case such alteration
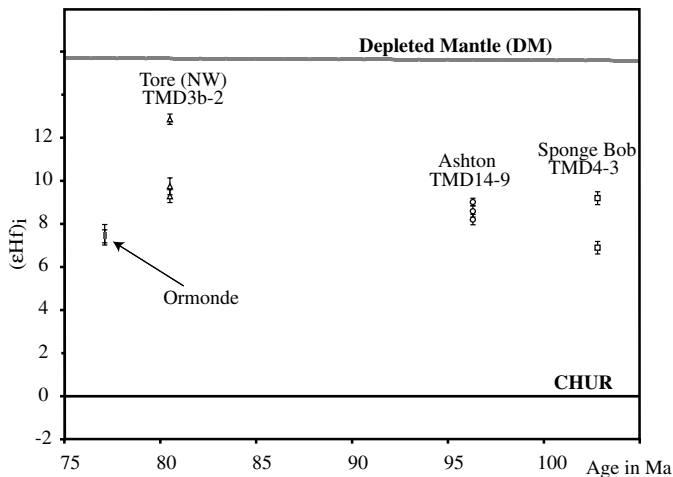
Fig. 11. Initial Hf isotopes signatures in relation to U–Pb ages of the different seamounts. For comparison, the evolution line of a chondritic mantle reservoir (CHUR) and an increasingly depleted mantle (DM) are plotted.

caused an increase in Rb/Sr leading to over-corrected initial ratio.

A plot of initial Sr and Pb isotope signatures reveals that three of our seamount samples (Jo Sister and Sponge Bob) are more radiogenic in ^{206}Pb than MORB, and two samples are less radiogenic in ^{87}Sr. These three rocks are a trachy-andesite (TMD16-1), a tephri-phonolite (TMD16-2), and a trachyte (TMD4-8). To evaluate the influence of potential bias by seawater alteration, we have calculated maximal shifts of initial ^{87}Sr/^{86}Sr. We used 5–10% Rb/Sr fractionation that corresponds to the extent of maximal observed feldspar alteration. This test shows that the ratios are affected to a very low degree only. For example, sample TMD16-1 corrected for 10% Rb/Sr-fractionation yields a minimum (^{87}Sr/^{86}Sr)$_i$ of 0.70271 and a maximum (^{87}Sr/^{86}Sr)$_i$ of 0.70287, compared to the original value of 0.70280 (Table 6). The other five trachy-andesites and trachytes plot in the Atlantic MORB field as do Pb–Sr data from Ormonde and Serra de Monchique (Fig. 10c).

Zircons from three of the dated rocks were analyzed for their initial Hf isotope composition to help constrain potential magma sources. Three zircon fractions were measured for the trachyte samples TMD3b-2 and TMD14-9, and two for the TMD4-3 trachyte. Initial epsilon Hf values (εHf$_i$) ranging from +6.9 to +12.9 (Table 7; Fig. 11) lie in-between the CHUR evolution line and a MORB type reservoir (DM). It is important to note that differences exist in epsilon Hf between zircon fractions of a given sample that are much in excess of the analytical uncertainty. These differences could result from: (1) mixing of magma batches, each containing zircon crystals at the time of mixing, (2) incorporation of xenocrystic zircon by extraction from adjacent wallrocks in a magma already containing zircon, and (3) a successively adding relatively small volume of isotopically distinct melts to a large volume of magma with a uniform isotope composition, coupled with new zircon growth at, or shortly after the time of mixing. In any case,
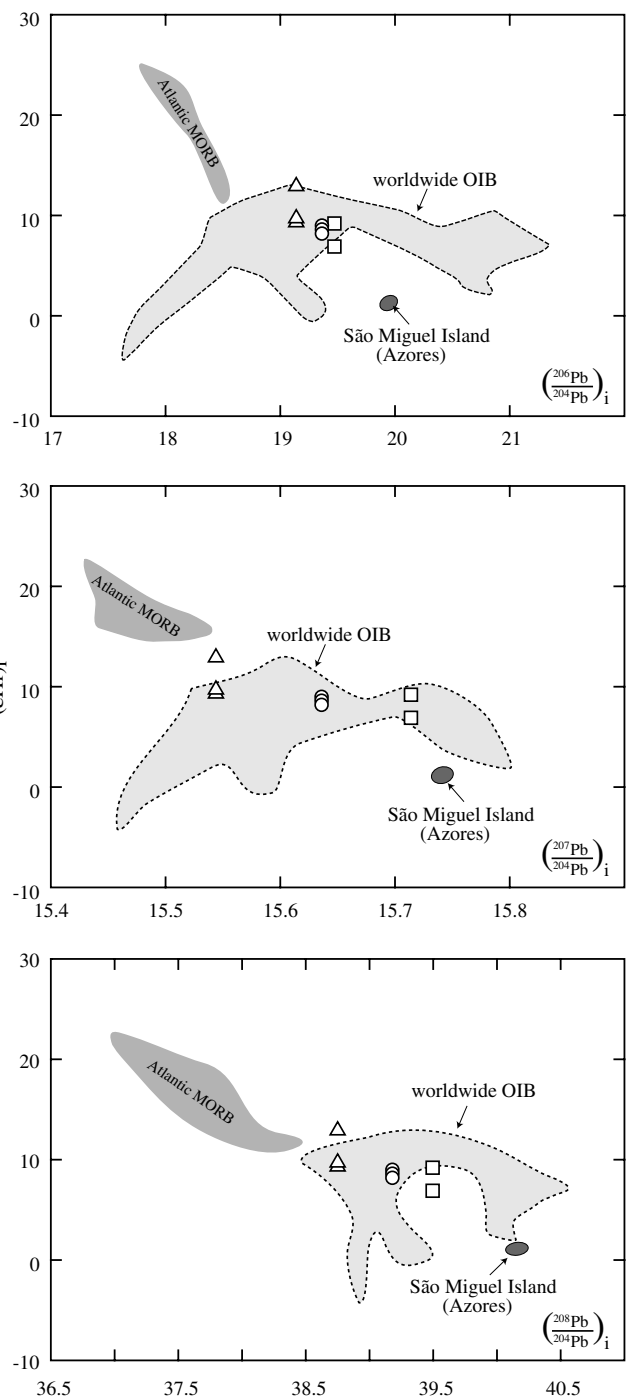

Fig. 12. Feldspar initial Pb vs. zircon initial Hf isotope signatures of the different seamount samples, compared to the present day data fields of Atlantic MORB (Salters and White, 1998; Nowell et al., 1998), worldwide OIB (Salters and White, 1998; Lassiter et al., 2003), and the São Miguel Island (Snyder et al., 2004).

this observation of differences in initial Hf signatures of zircon is consistent with the presence of small inherited radiogenic Pb components necessarily carried by relic zircons (Figs. 6a and 7a) that also requires extraction of grains from a different host. This host must have been significantly older than the magma, to explain inheritance in zircon, already observed in the 77 Ma old alkali rock on Ormonde (Fig. 11).

Fig. 12 shows correlations between initial Hf and Pb isotope signatures measured in the seamounts, plotted relative to the fields of Atlantic MORB, worldwide Ocean Island Basalts (OIB), and São Miguel Island. All our alkaline volcanic lavas are distinct from both Atlantic MORB and São Miguel volcanic rocks but they lie within the field of OIB sources.

8.4. Geodynamic context of magmatism

From a regional point of view, Cretaceous volcanoes roughly follow the significantly older J anomaly but also the different branches of the Azores-Gibraltar Fracture Zone (AGFZ; Fig. 1). This suggests these structures have played a major role for enabling magma ascent. An age difference of 7.8 ± 4.2 Ma observed for the two localities of the Tore seamount complex substantiates the hypothesis that its construction includes at least two distinct magmatic pulses. Since the two localities lie in the vicinity of the northern branch of the Azores-Gibraltar Fracture Zone (AGFZ in Fig. 1), magmatic activity could have been focused along the fault. It may also be that age gradients exist along faults such as suggested earlier by Féraud et al. (1977). Another useful observation is that formation of the seamounts between Tore and Jo Sister, and possibly up to the Madeira Archipelago, approximately follows the main direction of initial ocean spreading marked by the J anomaly (125–130 Ma) formed about 20 m.y. prior to first alkaline volcanism at 104 ± 1 Ma (Fig. 1). The boundary between the stretched continental lithosphere of Iberia and the oceanic lithosphere can be considered as a zone of weakness, and magmas can preferentially percolate through this zone, compared to normal oceanic or continental lithosphere. It is likley that this zone of weakness served as a guide for magma ascent and orientation of seamount emplacement. In extrapolating the actual spreading rate of 2.2 cm/y (DeMets et al., 1990) to Upper Cretaceous time, the Atlantic ridge would have been located about 460 km to the west at the time of volcanism at 104 Ma, using the 125–130 Ma initiation age for beginning Atlantic opening (Gradstein et al., 2004). On the other hand, if a very slow initial spreading rate of 0.67 cm/y is used (Srivastava et al., 2000) the distance would have been only 134 km.

From our new ages we cannot see any significant regional age trend along the seamount chain lying to the north of the Azores-Gibraltar-Fracture-Zone (AGFZ; Fig. 1). The same is true if we include the earlier dated 77 Ma old alkaline magmas on the Ormonde seamount and the 72 Ma old Serra de Monchique on the continent (Fig. 1). Given analytical uncertainties on these ages some minor regional age-trends may exist; however, they necessarily would lie within a few million years. An illustration for this are the three ages of the Tore seamounts (88.2 ± 3.9; 88.3 ± 3.3; 80.5 ± 0.9 Ma) where any age trend is necessarily limited to a few million years. Moreover, potential migration of volcanism north of the AGFZ must be compatible with motions of the Iberian plate at that time. Different hypotheses were proposed for movements of Iberia between 120 and 80 Ma, converging toward an agreement that it moved in southeast direction by about 800 km (e.g., Malod, 1989; Olivet, 1996; Sibuet et al., 2004b). Since we cannot see the corresponding age trend in our volcanoes, i.e., the absence of ages becoming increasingly younger towards the northwest, a Hawaiian-type plume model can be ruled out. This excludes the northern part of the Tore-Madeira Rise to be the simple volcanic trace of Iberian motion over such a hot spot between 120 and 80 Ma. Concerning the Tore-Madeira Rise region to the south of the AGFZ, the Oligocene–Miocene Unicorn, Ampere, and Seine volcanoes do not match the axis of the rise, lying significantly to the east (Fig. 1). Their emplacement most likely reflects a particular geodynamic context, possibly in relation to lithospheric discontinuities such as expressed by the large E–W striking faults in this region (Fig. 1) as suggested previously by Geldmacher et al. (2005). An alternative hypothesis considers these seamounts to belong to the Madeira hot-spot track across the African plate, spanning the Madeira Archipelago through the Unicorn, Seine, Ampere and Ormonde seamounts to the Serra de Monchique alkaline complex (Geldmacher et al., 2000, 2005; Geldmacher and Hoernle, 2000).

To explain the large extent of alkaline magmatism in the eastern North Atlantic (Fig. 1) migration of melting within the head region of a long lived thermal anomaly seems to be the most likely model. Such activity since at least 104 Ma (oldest seamount) to recent times (Madeira Archipelago) would be consistent with the persistent existence of large plumes, reaching life times of 130 m.y. (e.g., Courtillot et al., 2003). This would mean that the same thermal anomaly was/is periodically active underneath the Atlantic oceanic crust, the transition zone, and the continental margin of Iberia. Finite-frequency tomography indicates the presence of a deep-rooted plume (>1000 km depth) having maxima P-wave anomalies at about 300 km depth, underneath the Azores, Canary, and Madeira complexes (Montelli et al., 2004). This assumption is also valid in space and time if the about 300 km W–E anti-clockwise rotation of the Iberian Peninsula is considered.

8.5. Origin of magmas

In considering the full set of new data it seems that 104–81 Ma alkaline magmas were derived from sources having a component with: (1) low Rb/Sr, (2) relatively high epsilon Hf and (3) relatively high $^{207}Pb/^{204}Pb$ at a given $^{206}Pb/^{204}Pb$ (Figs. 10–12). To acquire such isotopic signatures, the magma sources must have evolved in isolation for several hundred million years. In any model explaining the genesis of our alkaline magmas, a contribution of crustal material is required to explain radiogenic Pb, and in particular the presence of inherited old radiogenic Pb

discovered in zircon (Figs. 6a and 7a). The most likely explanation is the incorporation of very minor amounts of detrital sediments, assimilation of lower continental crust or lithospheric mantle containing relic detrital sediments. The observed decoupling of Hf–Sr from Pb signatures is entirely consistent with the fact that mantle melts can very easily be shifted in Pb by addition of even very small amounts (a few %) of continental material (e.g., Schärer, 1991). This is not the case for Hf and Sr for which mantle melts have a strong buffering effect.

Interaction of OIB-type magmas with material from the Iberian lithospheric mantle seems to be the most plausible interpretation, satisfying the presence of Rb-depleted lithospheric mantle, highly radiogenic Pb, and inherited Pb in zircon. Supporting evidence in favor of this hypothesis are Sr data from the peridotite ridge about 500 km off the coast of Iberia (Fig. 1) where $^{87}Sr/^{86}Sr$ as low as 0.7021 were observed in Cpx in lherzolites, representing potential contaminating material of our magmas (Chazot et al., 2005). It has been shown that isotopic heterogeneity of Iberian margin ultramafic rocks were already present at the time of rifting, reflecting a long and complex history of depletion and enrichment events affecting old mantle (Chazot et al., 2005). We emphasize that this model concerns alkaline volcanic activity investigated here, i.e., the northern section of the Tore-Madeira Rise north of the Azores-Gibraltar Fracture Zone (Fig. 1). It is also be valid for the origin of the contemporaneous alkaline rocks on Ormonde and at continental Monchique, as well as the seamounts Ampere, Seine and Unicorn (Bernard-Griffiths et al., 1997; Geldmacher and Hoernle, 2000; Schärer et al., 2000; Geldmacher et al., 2005).

Given the geochemical and isotopic data for the northern part of Tore-Madeira Rise (Figs. 9, 10 and 12) we cannot reliably deduce mixing proportion between the OIB-type component, materials from the Iberian lithospheric mantle, and the necessarily very small amounts of crustal components present within or attached to the lithospheric mantle. This three components hypothesis applies to the seamounts composing the northern Tore Madeira rise volcanoes. On the other hand, sources of alkaline magmas to the South may vary, either along the rise or in neighbouring regions where alkaline volcanism occurs such as Seine, Ampere, and Ormonde (Fig. 1). Such differences were proposed for the origin of the latter seamounts as well as the Madeira Archipelago, where the involvement of a young high-U/Pb plume was proposed, interacting with enriched material present in the oceanic lithosphere possibly containing some continental material (Geldmacher and Hoernle, 2000; Geldmacher et al., 2005).

9. Major conclusions

(1) U–Pb ages of six seamount complexes emplaced along an about 500 km long segment of the northern Tore-Madeira Rise yield ages between 104 and 81 Ma, being significantly different in age than previously assumed. Their origin is not related to 130–125 Ma initiation of opening of the Atlantic ocean.

(2) A long-lived thermal anomaly, present underneath the continental plate margin since at least 104 Ma seems required to explain mantle melting and related volcanism. At the time of alkaline volcanism, the active Atlantic spreading center was located between 136 and 460 km to the West, corresponding to potential minimum and actually measured spreading rates of 0.67 and 2.2 cm/yr, respectively.

(3) Magmas were probably generated in the head of a mantle plume (OIB-type magmas) with time–space migrating domains of melting under the oceanic lithosphere, the ocean–continent transition zone and the continent. Small portions of continental material have also been incorporated in the magmas.

References

Allègre, C.J., Manhès, G., Göpel, C., 1995. The age of the Earth. *Geochim. Cosmochim. Acta* **59**, 1445–1456.

Bernard-Griffiths, J., Gruau, G., Cornen, G., Azambre, B., Macé, J., 1997. Continental lithospheric contribution to alkaline magmatism: isotopic (Nd, Sr, Pb) and geochemical (REE) evidence from Serra de Monchique and Mount Ormonde Complexes. *J. Petrol.* **38**, 115–132.

Beslier, M.-O., Girardeau, J., Boillot, G., 1988. Lithologie et structures des péridotites à plagioclase bordant la marge continentale passive de la Galice (Espagne). *C.R. Acad. Sci. Paris* **306**, 373–380.

Beslier, M.-O., Ask, M., Boillot, G., 1993. Ocean-continent boundary in the Iberia Abyssal Plain. *Tectonophysics* **218**, 383–393.

Blichert-Toft, J., Albarède, F., 1997. Lu–Hf isotope geochemistry of chrondrites and the evolution of mantle–crust system. *Earth Planet. Sci. Lett.* **148**, 243–258.

Blichert-Toft, J., Chauvel, C., Albarède, F., 1997. Separation of Hf and Lu for high-precision isotope analysis of rock samples by magnetic sector-multiple collector ICP-MS. *Contrib. Mineral. Petrol.* **127**, 248–260.

Bodet, F., Schärer, U., 2000. Evolution of the SE-Asian continent from U–Pb and Hf isotopes in single grains of zircon and baddeleyite from large rivers. *Geochim. Cosmochim. Acta* **64**, 2067–2091.

Boillot, G., Feraud, G., Recq, M., Girardeau, J., 1989. Undercrusting by serpentinite beneath rifted margins. *Nature* **341**, 523–525.

Boillot, G., Agrinier, P., Beslier, M.-O., Cornen, G., Froitzheim, N., Gardien, V., Girardeau, J., Gil Ibarguchi, J., Kornprobst, J., Moullade, M., Schärer, U., Vanney, J.-R., 1995. A lithospheric syn-rift shear zone at the ocean–continent transition preliminary results of the GALINAUTE II cruise (Nautile dives on the Galicia Bank, Spain). *C.R. Acad. Sci. Paris* **321**, 1171–1178.

Borsi, L., Schärer, U., Gaggero, L., Crispini, L., 1996. Age, origin and geodynamic significance of plagiogranite in lherzolithes and gabbros of the Piedmont–Ligurian ocean basin. *Earth Planet. Sci Lett.* **140**, 227–241.

Carignan, J., Hild, P., Mevelle, G., Morel, J., Yeghicheyan, D., 2001. Routine analyses of trace element in geological samples using flow injection and low pressure on-line liquid chromatography coupled to ICP-MS: a study of geochemical reference materials BR, DR-N, UB-N, AN-G and GH. *Geostand. Newsl.* **25**, 187–198.

Chazot, G., Charpentier, S., Kornprobst, J., Vannucci, R., Luais, B., 2005. Lithospheric mantle evolution during continental break-up: the West Iberia non-volcanic passive margin. *J. Petrol.* **46**, 2527–2568.

Cohen, R.S., O'Nions, R.K., Dawson, J.B., 1984. Isotope geochemistry of xenoliths from East Africa: implications for development of mantle reservoirs and their interaction. *Earth Planet. Sci. Lett.* **68**, 209–220.

Condomines, M., Tanguy, J.C., Kieffer, G., Allègre, C.J., 1982. Magmatic evolution of a volcano using 230Th–238U and trace elements systematics, the Etna case. *Geochim. Cosmochim. Acta* **46**, 1397–1416.

Cornen, G., 1982. Petrology of the alkaline volcanism of Gorringe Bank (southwest Portugal). *Mar. Geol.* **47**, 101–130.

Cornen, G., Girardeau, J., Monnier, C., 1999. Basalts, underplated gabbros and pyroxenites record the rifting process of the West Iberian margin. *Mineral. Petrol.* **67**, 111–142.

Cotten, J., Le Dez, A., Bau, M., Caroff, M., Maury, R.C., Dulsky, P., Fourcade, S., Bohn, M., Brousse, R., 1995. Origin of anomalous rare-earth elements and yttrium enrichments in subaerially exposed basalts: evidence from French polynesia. *Chem. Geol.* **119**, 115–138.

Courtillot, V., Davaille, A., Besse, J., Stock, J., 2003. Three distinct types of hotspots in the Earth's mantle. *Earth Planet. Sci. Lett.* **205**, 295–308.

DeMets, C., Gordon, R.G., Argus, D.F., Stein, S., 1990. Current plate motions. *Geophys. J. Int.* **101**, 425–478.

Féraud, G., Bonnin, J., Olivet, J.-L., Auzende, J.-M., Bougault, H., 1977. Sur quelques datations du volcanisme alcalin de la ligne Açore-Gibraltar et leur contexte géodynamique. *C.R. Acad. Sci. Paris, Sér. D* **285**, 1203–1206.

Féraud, G., Schmincke, H.U., Lietz, J., Gastaud, J., Pritchard, G., Bleil, U., 1981. New K–Ar ages, chemical analyses and magnetic data of rocks from the islands of Santa Maria (Azores), Porto Santo and Madeira (Madeira Archipelago) and Gran Canaria (Canary Islands). *Bull. Volcanol.* **44**, 359–375.

Féraud, G., Gastaud, J., Auzende, J.-M., Olivet, J.-L., Cornen, G., 1982. 40Ar/39Ar ages for the alkaline volcanism and basement of Gorringe Bank, North Atlantic Ocean. *Earth Planet. Sci. Lett.* **57**, 211–226.

Féraud, G., York, D., Mevel, C., Cornen, G., Hall, C.M., Auzende, J.M., 1986. Additional 40Ar/39Ar dating of the basement and the alkaline volcanism of Gorringe Bank (Atlantic Ocean). *Earth Planet. Sci. Lett.* **79**, 255–269.

Féraud, G., Girardeau, J., Beslier, M.O., Boillot, G., 1988. Datation 40Ar/39Ar de la mise en place des peridotites bordant la marge de la Galice (Espagne). *C.R. Acad. Sci. Paris II* **307**, 49–55.

Geldmacher, J., Van den Bogaard, P., Hoernle, K., Schmincke, H.U., 2000. The 40Ar/39Ar age dating of the Madeira Archipelago and hot spot track (eastern North Atlantic). *Geochem. Geophys. Geosyst.* **1**.

Geldmacher, J., Hoernle, K., 2000. The 72 Ma geochemical evolution of the Madeira hot spot (eastern North Atlantic): recycling of Paleozoic (500 Ma) oceanic lithosphere. *Earth Planet. Sci. Lett.* **183**, 73–92.

Geldmacher, J., Hoernle, K., 2001. Corrigendum to: The 72 Ma geochemical evolution of the Madeira hot spot (eastern North Atlantic): recycling of Paleozoic (500 Ma) oceanic lithosphere. *Earth Planet. Sci. Lett.* **186**, 333.

Geldmacher, J., Hoernle, K., Bogaard, P.v.d., Zankl, G., Garbe-Schönberg, D., 2001. Earlier history of the ⩾70 Ma old Canary hotspot based on the temporal and geochemical evolution of the Selvagen Archipelago and neighboring seamounts in the eastern North Atlantic. *J. Volcanol. Geotherm. Res.* **111**, 55–87.

Geldmacher, J., Hoernle, K., Van den Bogaard, P., Duggen, S., Werner, R., 2005. New 40Ar/39Ar age geochemical seamounts Canary and Madeira volcanic provinces: Support for the mantle plume hypothesis. *Earth Planet. Sci. Lett.* **237**, 85–101.

Geldmacher, J., Hoernle, K., Klügel, A., Van den Bogaard, P., Wombacher, F., Berning, B., Origin and geochemical evolution of the Tore-Madeira Rise (eastern North Atlantic), *J. Geophys. Res.* in press.

Girardeau, J., Cornen, G., Beslier, M.O., Le Gall, B., Monnier, C., Agrinier, P., Dubuisson, G., Pinheiro, L., Ribeiro, A., Whitechurch, H., 1998. Extensional tectonics in the Gorringe Bank rocks, Eastern Atlantic Ocean: evidence of an oceanic ultra-slow mantellic accreting center. *Terra Nova* **10**, 330–336.

Govindaraju, K., Mevelle, G., 1987. Fully automated dissolution and separation methods for inductively coupled plasma atomic emission spectrometry rock analysis. Application to the determination of rare earth elements. *J. Anal. Atom. Spectrom.* **2**, 615–621.

Gradstein, F.M., Ogg, J.G., Smith, A.G., 2004. *A geological time scale.* Cambridge University Press, Cambridge.

Halliday, A.N., Davies, G.R., Lee, D.C., Tommasini, S., Paslick, C.R., Fitton, J.G., James, D.E., 1992. Lead isotopic evidence for young trace element enrichment in the oceanic upper mantle. *Nature* **359**, 623–627.

Halliday, A.N., Davies, G.R., Lee, D.C., Tommasini, S., Paslick, C.R., Fitton, J.G., James, D.E., 1993. Correction to "Lead isotopic evidence for young trace element enrichment in the oceanic upper mantle". *Nature* **362**, 184.

Halliday, A.N., Lee, D.C., Tommasini, S., Davies, G.R., Paslick, C.R., Fitton, J.G., James, D.E., 1995. Incompatible trace elements in OIB and MORB and source enrichment in the sub-oceanic mantle. *Earth Planet. Sci. Lett.* **133**, 379–395.

Hoernle, K., Schmincke, H.U., Tilton, G., 1991. Sr, Nd and Pb isotope geochemistry of volcanics from Madeira and Porto Santo Islands, North Atlantic Ocean. *EOS Trans. Am. Geophys. Union* **72**, 528.

Hoernle, K., Zhang, Y.S., Graham, D., 1995. Seismic and geochemical evidence for large-scale mantle upwelling beneath the eastern Atlantic and western and central Europe. *Nature* **374**, 34–39.

Hoernle, K., and scientific party (2003) Cruise report M51/1. In: C. Hemleben, K. Hoernle, B.B. Jörhensen, W. Roether. (Eds.), Meteor Berichte 03-1, Univ. Hamburg, Germany, 3–35.

Holmes, A., 1946. An estimate of the age of the Earth. *Nature* **157**, 680–684.

Jaffey, H., Flynn, K.F., Glendenin, L.E., Bentley, W.C., Essling, A.M., 1971. Precision measurements of half-lives and specific activities of 235U and 238U. *Phys. Rev.* **C4**, 1889–1906.

Jiménez-Munt, I., Fernàndez, M., Torne, M., Bird, P., 2001. The transition from linear to diffuse plate boundary in the Azore-Gibraltar region: results from a thin-sheet model. *Earth Planet. Sci. Lett.* **192**, 175–189.

Krogh, T.E., 1973. A low contamination method for hydrothermal decomposition of zircon and extraction of U and Pb for isotopic ages determination. *Geochim. Cosmochim. Acta* **37**, 485–494.

Krogh, T.E., 1982. Improved accuracy of U–Pb zircon ages by the creation of more concordant systems using air abrasion technique. *Geochim. Cosmochim. Acta* **46**, 637–649.

Lassiter, J.C., Blichert-Toft, J., Hauri, E.H., Barsczus, H.G., 2003. Isotope and trace elements variations in lavas from Raivavae and Rapa, Cook-Austral islands: constraints on the nature of the HIMU-and EM-mantle and the origin of mid-plate volcanism in French Polynesia. *Chem. Geol.* **202**, 115–138.

Laughton, A.V., Roberts, D.G., Graves, R., 1975. Bathymetry of the northeast Atlantic: mid-Atlantic ridge to southwest Europe. *Deep Sea Res.* **22**, 791–810.

Le Bas, M.J., Le Maitre, R.W., Streckeisen, A., Zanettin, B., 1986. A chemical classification of volcanic rocks based on the total alkali-silica diagram. *J. Petrol.* **27**, 745–750.

Ludwig, K.R., 2003. User's Manual for Isoplot 3.00. Berkeley Geochronology Center Special Publication, 74pp.

Malod, J.A., 1989. Ibérides et plaque ibérique. *Bull. Soc. Géol. France* **5**, 927–934.

Manhès, G., Minster, J.F., Allègre, C.J., 1978. Comparative U–Th–Pb and Rb–Sr study of the Saint Séverin amphoterite: consequence for early solar system chronology. *Earth Planet. Sci. Lett.* **39**, 14–24.

Mata, J., Kerrich, R., MacRae, N.D., Wu, T.W., 1998. Elemental and isotopic (Sr, Nd and Pb) characteristics of Madeira Island basalts: evidence for a composite HIMU-EMI plume fertilizing lithosphere. *Can. J. Earth Sci.* **35**, 980–997.

Mauffret, A., Mougenot, D., Miles, P.R., Malod, J., 1989. Cenozoic deformation and Mesozoic abandoned spreading center in the Tagus Abyssal Plain (West of Portugal). *Can. J. Earth Sci.* **26**, 1101–1123.

McIntyre, R.M., 1977. Anorogenic magmatism, plate motion and Atlantic evolution. *J. Geol. Soc. Lond.* **133**, 375–384.

McIntyre, R.M., Berger, G.W., 1982. A note on the geochronology of the Iberian Alkaline Province. *Lithos* **15**, 133–136.

Merle, R., Caroff, M., Girardeau, J., Cotten, J., Guivel, C., 2005. Segregation vesicles, cylinders, and sheets in vapor-differentiated pillow lavas: examples from Tore-Madeira Rise and Chile Triple Junction. *J. Volcanol. Geotherm. Res.* **141**, 109–122.

Middlemost, A.E.K., 1989. Iron oxidation ratios, norms and the classification of the volcanic rocks. *Chem. Geol.* **77**, 19–26.

Minster, J.F., Ricard, L.P., Allègre, C.J., 1979. 87Rb–87Sr chronology of enstatite meteorites. *Earth Planet. Sci. Lett.* **44**, 420–440.

Miyashiro, A., 1978. Nature of alkaline volcanic rock series. *Contrib. Mineral. Petrol.* **66**, 91–104.

Montelli, R., Nolet, G., Dahlen, F.A., Masters, G., Engdahl, E.R., Hung, S.H., 2004. Finite-frequency tomography reveals a variety of plume in the mantle. *Nature* **303**, 338–343.

Moreira, M., Doucelance, R., Kurz, M.D., Dupré, B., Allègre, C.J., 1999. Helium and lead isotope geochemistry of the Azores Archipelago. *Earth Planet. Sci. Lett.* **169**, 189–205.

Nowell, G.M., Kempton, P.D., Noble, S.R., Fitton, J.G., Saunders, A.D., Mahoney, J.J., Taylor, R.N., 1998. High-precision Hf isotope measurements of MORB and OIB by thermal ionization mass spectrometry: insight into the depleted mantle. *Chem. Geol.* **149**, 211–233.

Olivet, J.-L., 1996. La cinématique de la plaque Ibérique, Bull. *Centres Rech. Explor.-Prod. Elf Aquitaine* **20**, 131–195.

Patchett, P.J., Tatsumoto, M., 1980. A routine high-precision method for Lu–Hf isotope geochemistry and chronology. *Contrib. Mineral. Petrol.* **75**, 263–267.

Patchett, P.J., Kouvo, O., Edge, C.E., Tatsumoto, M., 1981. evolution of continental crust and mantle heterogeneity: Evidence from Hf isotopes. *Contrib. Mineral. Petrol.* **78**, 279–297.

Peirce, C., Barton, P.J., 1991. Crustal structure of the Tore-Madeira Rise, Eastern North Atlantic-results of a DOBS wide-angle and normal incidence seismic experiment in the Josephine Seamount region. *Geophys. J. Int.* **106**, 357–378.

Pinheiro, L.M., Whitmarsh, R.B., Miles, P.R., 1992. The Ocean-Continent boundary off the western continental margin of Iberia. II. Crustal structure in the Tagus Abyssal Plain. *Geophys. J. Int.* **109**, 106–124.

Pitman III, W.C., Talwani, M., 1972. Sea-floor spreading in the North Atlantic. *Geol. Soc. Am. Bull.* **83**, 619–646.

Rock, N.M.S., 1976. The comparative strontium isotopic composition of alkaline rocks: new data from southern Portugal and east Africa. *Contrib. Min. Petrol.* **56**, 205–228.

Rock, N.M.S., 1982. The late Cretaceous alkaline igneous province in the Iberian peninsula, and its tectonic significance. *Lithos* **15**, 111–131.

Roest, W.R., Danobeitia, J.J., Verhoef, J., Colette, B.J., 1992. Magnetic anomalies in the Canary basin and the Mesozoic evolution of the Central North Atlantic. *Mar. Geophys. Res.* **14**, 1–24.

Salters, V.J.M., White, W.M., 1998. Hf isotope constraints on mantle evolution. *Chem. Geol.* **145**, 447–460.

Schärer, U., 1991. Rapid continental crust formation at 1.7 Ga from a reservoir with chondritic isotope signatures, eastern Labrador. *Earth Planet. Sci. Lett.* **102**, 110–133.

Schärer, U., Kornprobst, J., Beslier, M.O., Boillot, G., Girardeau, J., 1995. Gabbro and related rocks emplacement beneath rifting continental crust: U–Pb geochronological an d geochemical constraints for the Galicia passive margin (Spain). *Earth Planet. Sci. Lett.* **130**, 187–200.

Schärer, U., Girardeau, J., Cornen, G., Boillot, G., 2000. 138–121 Ma asthenospheric magmatism prior to continental break-up in the North Atlantic and geodynamic implications. *Earth Planet. Sci. Lett.* **181**, 555–572.

Sguigna, A.P., Larabee, A.J., Waddington, J.C., 1982. The half-life of 176Hf by ã-ã coincidence measurements. *Can. J. Phys.* **60**, 361–364.

Sibuet, J.C., Monti, S., Loubrieu, B., Mazé, J.P., Srivastava, S., 2004a. Carte bathymètrique de l'Atlantique nord-est et du golfe de Gascogne: implications géodynamiques. *Bull. Soc. Géol. France* **175**, 429–442.

Sibuet, J.-C., Srivastava, S., Spakman, W., 2004b. Pyrenean orogeny and plate kinematics. *J. Geophys. Res.* **108**, B08104.

Snyder, D.C., Widom, E., Pietruszka, A.J., Carlson, R.W., 2004. The role of open-system processes in the development of silicic magma chambers: a chemical and isotopic investigation of the Fogo A trachyte deposit, Sao Miguel, Azores. *J. Petrol.* **45**, 723–738.

Srivastava, S.P., Sibuet, J.-C., Cande, S., Roest, W.R., Reid, I.D., 2000. Magnetic evidence for slow seafloor spreading during the formation of the Newfoundland and Iberian margins. *Earth Planet. Sci. Lett.* **182**, 61–76.

Stacey, J.S., Kramers, J.D., 1975. Approximation of terrestrial lead isotope evolution by a two-stage model. *Earth Planet. Sci. Lett.* **26**, 207–221.

Steiger, R.H., Jäger, E., 1977. Subcommission on geochronology: convention on the use of decay constants in geo- and cosmochronology. *Earth Planet. Sci. Lett.* **36**, 359–362.

Sun, S.S., McDonough, W.F., 1989. Chemical and isotopic systematics of oceanic basalts: implication for mantle composition and processes. In: Saunders, A.D., Norry, M.J. (Eds.), *Magmatism in the ocean basins*, vol. 42. Geol. Soc. Spec. Publ., London, pp. 313–345.

Tatsumoto, M., Knight, R.J., Allègre, C.J., 1973. Time differences in the formation of meteorites as determined from the ratio of 207-lead to 206-lead. *Science* **180**, 1279–1283.

Thirlwall, M.F., 1997. Pb isotopic and elemental evidence for OIB derivation from young HIMU mantle. *Chem. Geol.* **139**, 51–74.

Tucholke, B.E., Ludwig, W.J., 1982. Structure and origin of the J Anomaly Ridge, Western North Atlantic Ocean. *J. Geophys. Res.* **87**, 9389–9407.

Van der Linden, W.J.M., 1979. The Atlantic margin of Iberia and Morocco, a reinterpretation. *Tectonophysics* **59**, 185–199.

Villemant, B., Joron, J.-L., Jaffrezic, H., Treuil, M., Maury, R., Brousse, R., 1980. Cristallisation fractionnée d'un magma basaltique alcalin: la serie de la chaine des Puys (Massif Central, France) II: Géochimie. *Bull. Minéral.* **103**, 267–286.

Wendt, I., Kreuzer, H., Muller, P., Von Rad, U., Raschka, H., 1976. K–Ar age of basalts from Great Meteor and Josephine seamount (eastern North Atlantic). *Deep Sea Res.* **23**, 849–862.

Whitmarsh, R.B., Avedik, F., Saunders, M.R., 1986. The seismic structure of thinned continental crust in the northern Bay of Biscay. *Geo. J. Roy. Astr. Soc.* **86**, 589–602.

Widom, E., Carlson, R.W., Gill, J.B., Schmincke, H.U., 1997. Th–Sr–Nd–Pb isotope and trace elements evidence for the origin of Sao Miguel, Azores, enriched mantle source. *Chem. Geol.* **140**, 49–68.

Widom, E., Hoernle, K., Shirey, S.B., Schmincke, H.U., 1999. Os isotope systematics in the Canary Islands and Madeira: lithospheric contamination and mantle plume signature. *J. Petrol.* **40**, 279–296.

Zartman, R.E., Doe, B.R., 1981. Plumbotectonics—the model. *Tectonophysics* **75**, 135–162.

Zhang, L.S., Schärer, U., 1996. Inherited components in magmatic titanite and their consequence for the interpretation of U–Pb ages. *Earth Planet. Sci. Lett.* **138**, 57–65.